CALPHAD: Computer Coupling of Phase Diagrams and Thermochemistry 35 (2011) 427–445

Contents lists available at SciVerse ScienceDirect

CALPHAD: Computer Coupling of Phase Diagrams and Thermochemistry

journal homepage: www.elsevier.com/locate/calphad

An overview on phase equilibria and thermodynamic modeling in multicomponent Al alloys: Focusing on the Al–Cu–Fe–Mg–Mn–Ni–Si–Zn system

Yong Du [a,b,*], Shuhong Liu [a,b], Lijun Zhang [a], Honghui Xu [a,b], Dongdong Zhao [a], Aijun Wang [a], Liangcai Zhou [a]

[a] State Key Laboratory for Powder Metallurgy, Central South University, Changsha, Hunan, 410083, China
[b] Science Center for Phase Diagrams & Materials Design and Manufacture, Central South University, Changsha, Hunan, 410083, China

ARTICLE INFO

Article history:
Received 26 November 2010
Received in revised form
14 June 2011
Accepted 16 June 2011
Available online 16 July 2011

Keywords:
Al alloys
Thermodynamics
Phase diagram
CALPHAD
First-principles calculations

ABSTRACT

Knowledge of thermodynamics and phase diagram is a prerequisite for understanding many scientific and technological disciplines. To establish a reliable thermodynamic database, an integrated approach of key experiments and thermodynamic modeling, supplemented with first-principles calculations, can be utilized. In this paper, first investigations of phase diagram and thermodynamics of technologically important Al alloys (focusing on the Al–Cu–Fe–Mg–Mn–Ni–Si–Zn system, which covers the major elements in most commercial Al alloys) is reviewed with an emphasis on the need of the integrated approach. Second, the major experimental methods (X-ray diffraction, metallography, electron probe microanalysis, differential thermal analysis, diffusion couple method, and calorimetry), which are widely employed to provide phase diagram and thermodynamic data, are briefly described. Third, the basics of the first-principles calculations and CALPHAD are presented focusing on the integration of these two computational approaches. Case study for the representative Al–Fe–Ni ternary system is then demonstrated, followed by a thermodynamic modeling of the quinary Al–Fe–Mg–Mn–Si system and a brief summary to our recent activities on investigations of phase equilibria in multicomponent Al alloys.

1. Introduction

Al alloys are widely used in aerospace and civil industry. In the production of commercial Al alloys, knowledge of phase diagrams and thermodynamic properties is essential in defining processing conditions for optimal engineering properties. Thermodynamic properties are also needed to obtain the thermodynamic factor for a diffusion database development for simulation of microstructure evolution. The thermodynamic properties and database of multicomponent Al alloys have been under development for many years. Currently, there are two commercial thermodynamic databases for Al alloys, i.e. TT-Al [1] and PanAl [2]. It is important to understand the strengths and weaknesses of existing databases so that both users and developers of the databases can identify the critical work needed to improve the databases. It is generally believed that the thermodynamic descriptions of ternary systems are critical for the establishment of multicomponent thermodynamic database. Due to the lack of accurate experimental phase diagram and/or thermodynamic data, thermodynamic optimizations reported in the literature for many ternary systems of Al alloys were performed mainly by using early experimental data, such as the data published by Phillips et al. in the 1940s [3–6].

Among the huge number of publications on phase diagram measurements of Al alloys, representative work from several research groups could be addressed. As early as 1920s and 1930s, Dix Jr. and Heath Jr. [7,8] measured phase equilibria in several Al-based ternary systems, such as the Al–Fe–Si and Al–Mn–Si systems, using optical microscopy (OM) and X-ray diffraction (XRD) method. Almost during the same period, Gwyer and Phillips [9], Masing and Dahl [10], Fuss [11], Bückle [12], Bradley and Taylor [13] and Takeda and Mutuzaki [14] investigated the phase equilibria in some Al-based ternary systems by means of XRD, OM and thermal analysis (TA). In the 1940s and 1950s, Phillips et al. [3–6] Phragmen [15], Raynor et al. [16,17] and Nowotny et al. [18] published plentiful experimental data on the phase equilibria in Al-based ternary and quaternary systems. Although the pioneering work by the above researchers is emphasized in the literature, the phase relations published by them are considered to be only approximate. Our systematic experimental investigations and thermodynamic modeling [19] indicated that the liquidus temperatures in the Al–Mn–Si system measured by Phillips et al. [3–6] are substantially too low (at least 20 °C). Another problem associated with these early experimental data is the low purity of starting materials available at that time.

* Corresponding author at: State Key Laboratory for Powder Metallurgy, Central South University, Changsha, Hunan, 410083, China.
E-mail address: yongducalphad@gmail.com (Y. Du).

0364-5916/$ – see front matter © 2011 Elsevier Ltd. All rights reserved.
doi:10.1016/j.calphad.2011.06.007

From the 1950s to 1990s, the phase diagrams in Al alloys were subject of extensive measurements. Experimental phase diagram data and crystal structure data for the compounds in many Al-based ternary systems are critically reviewed in Landolt–Börnstein book series [20]. Another impressive attempt to establish the phase diagrams in Al alloys is the COST 507 project [21], the focus of which is the quinary Al–Fe–Mg–Mn–Si system and its subsystems. Belov et al. [22] presented comprehensive review on the experimentally measured multicomponent phase diagrams for commercial Al alloys. All of the experimental data mentioned in that book [22] are critically reviewed in our investigation for individual systems. The present review focused on the establishment of a thermodynamic database for multicomponent Al alloys via a hybrid approach of key experiment, CALPHAD and first-principles calculations instead of the extensive literature review. Generally speaking, since 1990 the thermodynamic modeling on Al alloys has been the major focus of many researchers, and systematically experimental determination of the phase diagrams in Al alloys has been rather limited [23–27].

Extensive literature survey [20] indicates that for most of Al-based ternary systems there are very limited or no thermodynamic data. Only for some key ternary systems of Al alloys, plentiful thermodynamic data are available. The Al–Fe–Si [28], Al–Mn–Si [19] and Al–Fe–Ni [29] systems are three of these systems. Our recent thermodynamic modeling on several Al-based ternary systems [19,28–31] demonstrates that it is possible to describe extensive phase diagram and all kinds of thermodynamic data by means of the optimized thermodynamic parameters. Thus it is expected that a reliable thermodynamic database for Al alloys can describe both thermodynamic properties and phase diagram data simultaneously.

A purely experimental approach to obtain an accurate phase diagram and thermodynamic properties for multicomponent Al-based system can be a very costly and lengthy process. Thermodynamic calculations via CALPHAD approach [32] can be used to reduce the amount of experimental effort required to treat the constantly growing list of commercial alloys. With descriptions for edge ternary systems, phase equilibria and thermodynamic quantities in higher-component systems can be computed via the standard procedure [33]. The prediction ability of this approach in a quaternary system critically depends on the quality for the thermodynamic descriptions of the constituent binary and ternary systems. The same is true of going from quaternary systems to a quinary one and so on. It could be mentioned that in the near future the CALPHAD approach will likely remain an important tool for the establishment of multicomponent phase diagrams and not a replacement for experiment. Another feature, which should be noticed, is that the thermodynamic parameters in CALPHAD approach can only be evaluated with experimental data. For the systems with high oxygen affinity and vapor pressure, it is extremely difficult to prepare alloys, which are suitable for experimental measurement of phase diagram and thermodynamic properties.

Recent advances in first-principles calculations based on density functional theory (DFT) have enabled one to compute thermodynamic and structural properties of phases using the atomic numbers and crystal structure information as input [34,35]. It has been demonstrated by Wolverton et al. [36,37] and Liu et al. [38,39] that first-principles calculations provide a reliable way of predicting thermodynamic data when such data are not available in the literature. Thus first-principles calculations can enrich the applications of CALPHAD approach.

Since precise thermodynamic descriptions permitting accurate predictions for phase equilibria and thermodynamic properties in higher order systems would make a big impact for further development of the multicomponent commercial Al alloys, a research project to establish a thermodynamic database for technologically important Al-based systems by means of a hybrid approach of key experiment, CALPHAD and first-principles calculation is in progress in our group [19,28–31]. Our work is perhaps the latest attempt to establish a high precision thermodynamic database for multicomponent Al alloys.

This review paper aims to summarize phase diagram and thermodynamics in multicomponent Al alloys mainly based on our research activities in the past several years. In Section 2, we briefly describe the major experimental methods (XRD, electron probe microanalysis (EPMA), differential thermal analysis (DTA), diffusion couple method, and calorimetry), which are employed to provide decisive phase diagram and thermodynamic data. The fundamentals of the first-principles calculations and CALPHAD are presented in Section 3 highlighting the integration of these two computational approaches. Case study for the representative Al–Fe–Ni ternary system is discussed in Section 4 with a desire to corroborate the developed methodology, followed by the thermodynamic description of the Al–Fe–Mg–Mn–Si quinary system and a brief introduction to our current activities on investigations of phase diagrams in multicomponent Al alloys.

2. Experimental methods for measurement of phase diagrams and thermodynamic properties

Currently, several techniques are utilized to determine phase diagrams. They include TA, metallography, XRD, dilatometry, electrical conductivity measurement and magnetic analysis methods, among others. All these methods are based on the principle that when a phase transition occurs in an alloy, its physical and chemical properties, phase composition and/or structure would vary. By analyzing the temperature and compositional changes associated with phase transitions, one can construct phase boundaries according to the phase rule. For the detailed descriptions of various methods to determine phase diagrams, reader is referred to one recent book by Zhao [40]. Although the introduction about these classical techniques can be found in many textbooks, there is no review paper which introduces these techniques in a compact way. In our brief introduction to these techniques, we have described several issues which should be taken into account according to our own experience.

This section will very briefly describe several important methods for measuring phase diagrams. No attempt is made to give an exhaustive review for these experimental methods. However, representative phase diagrams are presented to demonstrate the utilizations of these methods. Among the various methods to determine thermodynamic properties [41], only the widely employed calorimetry will be briefly described.

2.1. XRD

XRD [42] is widely used to determine the presence of phase(s) in an alloy under specified heat treatment and thus places the alloy in the phase region with the known composition of the phase(s), which is measured with either chemical analysis or EPMA. Another essential application of XRD is the determination of the crystal structure for a new phase [43]. One of the important tasks in the determination of binary, ternary and higher order phase diagrams is to find out whether there are compounds for the investigated systems. Quantitative determination of the amounts of different phases in multiphase mixtures can be done by peak-ratio calculations [42].

Currently, XRD data are automatically collected and analyzed. The preparation of a specimen for XRD analysis is usually the most critical factor influencing the quality of the result. The ideal specimen is a statistically significant amount of randomly

oriented powders with a crystallite size less than 10 μm, mounted in a manner without a preferred crystallite orientation. The preparation method of XRD powder specimens depends on the properties of the samples. Brittle samples can be easily fragmented and then grinded in agate mortars without cold-working induced internal stress. Thus prepared powder can be directly analyzed by XRD. High-ductility metallic samples can be made into powder by stainless files or diamond wheel grinding. If the sample is ferromagnetic, non-magnetic grinding wheel or stainless files can be used. The grinded powder specimens can then be successfully separated from the abrasive materials using a magnet. For an alloy with a strong ductility, a high internal stress may be induced by cold working, resulting in undesirable XRD peak broadening. Annealing treatment (so-called relief annealing) is required to remove this internal stress. The temperature for relief annealing is usually low (about 400 °C), and the annealed specimens should be slowly cooled to room temperature.

There are many cases where the observed phases have different brittleness and hardness. As a result, the sizes of the particles may differ significantly. After sieving, the relative content of each phase in the powder will change. Consequently, this kind of sample should be grinded until all the particles pass through the required screen mesh. During this process, one needs to avoid reaction of certain components in the alloy with oxygen or nitrogen in air or in the following annealing treatment. Oxygen or nitrogen may form interstitial solid solutions or even new phases with some components, and thus influence the accuracy of a phase diagram determination. Another process leading to the composition variation is preferential oxidation of some components in the alloy powders. In this case, the preparation of powders can be carried out in vacuum or an inert gas atmosphere, such as inside a glove box.

Phase identification is usually accomplished by comparing the peaks and relative intensities from the investigated specimen with those taken from a very large set of "standard" data provided by the International Center for Diffraction Data (ICDD) or other databases. Professional software, such as Jade (Materials Data, Inc., USA), can be used to access to this and other massive (and continually growing) databases. Jade includes an automated search-match function that compares XRD pattern of the sample with that from the ICDD database. With high quality XRD peaks from a single phase, the automated search-match program will usually identify the phase successfully. For most two-phase samples the identification of the dominant phase is usually successful with more hunting for the identification of the second phase. As the number of phase increases, the identification on all the phases is usually time-consuming. Fortunately the ability to visually compare the XRD patterns of the sample with those from a large number of possible phases is a manageable task.

Based on the XRD results, two methods, peak intensity method and lattice parameter method, are usually used for the determination of phase boundaries. The peak intensity method is widely used in the phase diagram determination. Different phases have different crystal structures that are characterized by their distinctive XRD peaks. The phases in an alloy can be determined by the XRD patterns to have either a single phase or multiple phases. The lattice parameter method for the determination of the phase boundary of a solid solution is very straightforward: plot the lattice parameter against the compositions of the alloys and find the composition at which the lattice parameter first becomes constant.

2.2. Metallography, scanning electron microscopy/energy dispersive x-ray microanalysis (SEM/EDX), and electron probe microanalysis (EPMA)

2.2.1. Metallography

Metallographic analysis, which is based on the assumption that the observed microstructure can represent the true structure of the samples, is one of the common tools for determining phase diagrams. Microstructure examinations are routinely used to investigate the number of phases and invariant reaction types. In particular, the characteristics of each phase, such as composition, size, shape, distribution, color, orientation and hardness, may be examined.

Prior to metallographic observation, the surface of a specimen should be cleaned and polished. Small samples are usually inlaid in polymer resin, mechanically grinded and finally subjected to polishing with emery paste of Al_2O_3, Cr_2O_3, Fe_2O_3, MgO or carborundum. Sometimes electrolytic polishing and electro-spark polishing are used. In order to clearly identify the microstructure, all kinds of etching methods are adopted to display the interfaces between different phases.

Optical microscopy (OM) is a classical technique for phase identification. Many phase diagrams published before the 1950s, including the phase diagrams of Al alloys, were determined using OM alone, as demonstrated in the pioneering work by Vogel [44] and Gayler [45]. There is one tremendous value in examining a sample optically since many phases can be easily observed in OM. An examination of a sample from low magnifications to high magnifications can provide some message about the phases, such as approximate volume fraction, microstructure type, homogeneity, and a potential surface contamination. The major limitations of OM are its limited magnification (usually $\leq 2000X$), which prevents its use for observation of fine microstructure feature, and the essential absence of information on the composition and crystal structure of the phases.

2.2.2. SEM/EDX and EPMA

Scanning electron microscopy (SEM) is one widely used tool for phase diagram determination. For the detailed description on the principle of SEM and its various applications, the reader is referred to the recent book by Goldstein et al. [46]. In SEM, a focused and collimated electron beam impinges upon the surface of a sample, creating backscattered electrons, secondary electrons, characteristic X-rays, and Auger electrons among other signals. By rasterizing the electron beam around a small rectangular area of the sample and putting a signal, such as secondary electron intensity, on a screen in a raster mode, a corresponding image is obtained. Two predominate imaging modes are backscattered electron (BSE) imaging and secondary electron imaging. The main contrast of BSE images comes from the difference in the average atomic number at each point in the sample. Such a contrast gives information on composition. Contrast mechanism for secondary electron imaging is predominately the surface topology of the sample with small contrast contribution from backscattered electrons. SEM is usually coupled with energy dispersive X-ray microanalysis (EDX). EDX is a microanalytical technique that uses the characteristic spectrum of X-rays emitted by the different elements in a specimen after excitation by high-energy electrons to obtain quantitative or qualitative information about the composition of a sample. When employed to measure a phase diagram, EDX can provide information on compositions of individual phases and the distribution of alloying elements. Sometimes the volume fractions of phases in a multiphase alloy need to be measured in order to establish a phase diagram. Images, which are representative of the whole sample, are taken and usually processed with imaging software to extract the volume fractions from the area proportions. With known densities and molar weight of the phases, the weight and mole fractions of the phases can be computed. In general, trace amount of phases can also be identified with this method. However, the imaging analysis software is prone to error in some case and should be carefully checked with other methods.

EPMA is another important technique for phase diagram determination. This technique yields more accurate composition for the targeted phase in comparison with SEM/EDX. For the exhaustive description on the principle of EPMA and its abundant applications, the reader is referred to the recent book by Reed [47]. EPMA is essentially a dedicated SEM with wavelength dispersive spectrometers (WDS) attached. As an elemental analysis technique, it uses a focused beam of high-energy electrons (5–30 KeV) in the SEM to impinge on a sample to induce emission of characteristic X-rays from each element. Its spatial resolution for X-ray microanalysis depends mainly on the accelerating voltage of the electron beam and the average atomic weight of a phase in a specimen, and usually ranges from one to several microns.

Quantitative matrix correction procedures have been well developed over the last several decades. These quantitative procedures have been demonstrated to produce error distributions characterized by a standard deviation of less than 3% relative when the samples are in the ideal form of a metallographically polished bulk solid. Standards utilized in EPMA are in the form of pure elements or compounds, such as MgO and GaP. This analytical approach provides a great versatility in the analysis of many elements with the exception of a few light elements (atomic numbers less than 6). Detection limits are of the order of 100 ppm. Spatial distribution of elemental constituents can be visualized quantitatively by digital composition maps and displayed in a gray scale or false colors.

The EPMA technique is mainly used to measure the phase boundaries of single phase, two phases, three phases and even multiphases. To determine the triangle of the three-phase equilibria with EPMA, only one alloy within the three-phase region is needed. The phase composition is measured when the electron beam hits the crystal grains of each of the three phases. Other techniques, such as XRD, would require more alloys to determine the phase boundaries through the lattice parameter *vs.* composition curves within single and two-phase regions. The EPMA measurement is far less time-consuming. For a two-phase equilibrium, crystal grains of each phase (in a range of several microns) are easily selected and analyzed by EPMA. The measurements yield tie lines. When the compositions of two phases are very close to each other, care should be taken in using EPMA for tie-line determination. In this case, a combination of EPMA with XRD or metallography should be used to determine a phase diagram accurately.

Using OM, XRD, SEM/EDX and EPMA methods, we have measured many ternary phase diagrams of the Al–Cu–Fe–Mg–Mn–Ni–Si–Zn system. Fig. 1 shows the isothermal section at 427 °C in the Al–Mg–Ni system measured with XRD and SEM/EDX methods [48]. SEM/EDX measurements on a few representative alloys are used to refine the phase boundaries resulting from XRD analysis. Fig. 2 shows the isothermal section at 800 °C in the Al–Cr–Si system measured mainly with SEM/EDX and EPMA methods [49].

Dynamic observation of phase change can be realized by installing heating and cooling stage on OM or SEM. By *in situ* investigation of solid-state phase transition, melting and crystallization of alloy samples during a heating or cooling process, plentiful information on phase relationships can be obtained.

2.3. Diffusion couple

The experimental determination of the phase diagrams is generally very time-consuming by means of equilibrated alloys, which are subjected to the above mentioned experimental methods. Our series of work demonstrates that a flexible combination of the diffusion couple technique with equilibrated alloys [50–55] is powerful and efficient in the determination of binary, ternary, and even quaternary phase diagrams. The

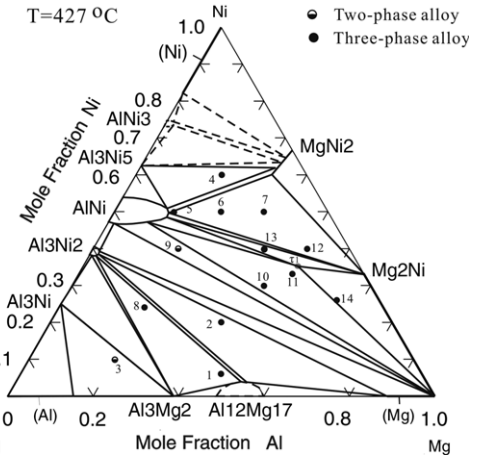

Fig. 1. Measured isothermal section of the Al–Mg–Ni system at 427 °C [48].

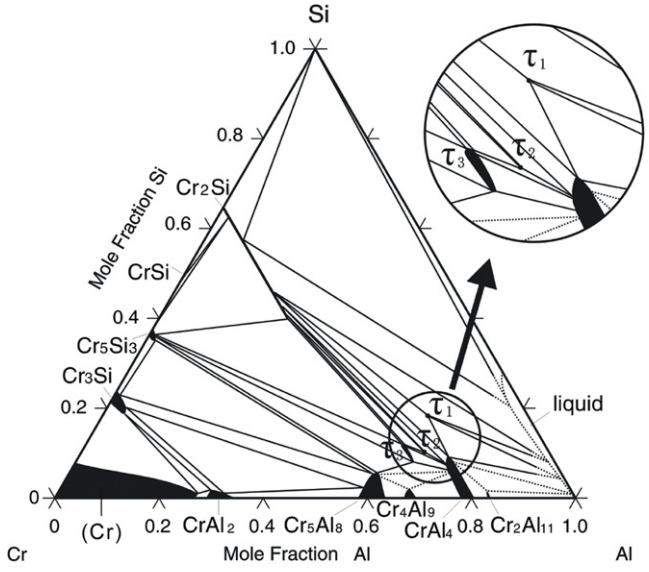

Fig. 2. Measured isothermal section of the Al–Cr–Si system at 800 °C [49].

sequence of the phases for a multiphase binary system, which are formed in the diffusion couples after interdiffusion at a given temperature, is dictated by the corresponding binary phase diagram [56]. For a ternary system, the microstructure of the diffusion zone can be visualized with the aid of the so-called diffusion path, which should keep to the law of mass conservation.

The use of diffusion couples in phase diagram studies is subjected to the assumption of a local equilibrium in the diffusion zone. Such a local equilibrium means that the interfacial reaction is very rapid in comparison with the rate of diffusion so that every infinitely thin layer of such a diffusion zone is in thermodynamic equilibrium with the nearby layers. In practice, the composition–distance curves for the elements are determined along a line perpendicular to the interfaces between every two adjacent phases in the diffusion couples using EPMA. The equilibrium composition of an individual phase is obtained by extrapolating the composition–distance curves for the elements to the phase boundaries. The end members of a ternary diffusion couple can be pure element or binary alloys. When the pure elements show quite different melting points, the diffusion couple consisting of a binary alloy and a third element is usually assembled.

The disadvantage of the diffusion couple technique is that it cannot generate phase transition temperatures and the liquid–

solid phase equilibrium data. Thus the diffusion couple technique is usually combined with equilibrated alloys to provide complete phase diagrams. Fig. 3(a) presents the isothermal section at 340 °C in the Al–Ni–Zn system by means of diffusion couple and equilibrated alloys [50]. After interdiffusion at 340 °C, the sequence of the phases that are formed in the diffusion couple $Al_{25}Ni_{75}$/Zn is generally $AlNi_3 \rightarrow \tau_1 \rightarrow \tau_2$ (→ crevice) → (Zn), as shown in Fig. 3(b). Nevertheless, more complex microstructure appears in a small portion of the diffusion area, as shown in the highlight of Fig. 3b. Usually in order to refine the phase relations resulting from the diffusion couple technique, representative alloys are prepared. For that purpose, 11 ternary alloys in the Al–Ni–Zn system are selected based on the approximate phase diagram established with the diffusion couple technique [50]. Fig. 3c shows the BSE image of one representative ternary alloy ($Al_{26}Ni_{13}Zn_{61}$) annealed at 340 °C for 480 h. The EPMA is used to determine the accurate tie-triangle of $Al_3Ni + Al_3Ni_2 + (Zn)$.

2.4. DTA and DSC

Many books are published on the introduction to DTA and DSC including principles, techniques and applications. The reader is referred to two books for the detail [40,57]. In the present review, no attempt is made to have an exhaustive compendium of the two methods. Instead, the principles of these methods and several important factors affecting the analysis of DTA and DSC are very briefly presented.

2.4.1. DTA

A phase transition usually involves an enthalpy change, and thermal properties are commonly monitored to detect this transition. When a specimen is heated or cooled under uniform conditions, a structural change will be identified with a temperature anomaly by plotting temperature versus time.

Two major techniques to detect phase transitions are developed based on enthalpy change [40,57]. The first one is thermal analysis (TA) where temperature versus time curve shows a thermal arrest at a phase transition point. The second technique is DTA in which a test sample and an inert reference sample are heated and cooled under the identical condition and a temperature difference between the test sample and reference one is recorded. Since the signal is differential during DTA measurement, it can be amplified with a suitable DC amplifier to attain an increased sensitivity. As a result, DTA is more sensitive than TA. The differential temperature is then plotted either against time or against temperature. When a phase transition takes place in a sample that involves release of heat, the temperature of the test sample rises temporarily above that of the reference sample, resulting in an exothermic peak. Conversely, a transition accompanied by absorption of heat reduces the temperature of the test sample compared to that of the reference sample, leading to an endothermic peak.

There are several factors influencing the shape of a DTA trace and these factors can be classified into three groups: the equipment variable, the sample variable and the experimental parameter. The first one includes factors, such as sample holder design and furnace design and they come with a choice of the apparatus. The sample variables, which can be directly controlled by an investigator, are the major factors that influence the result of DTA. They include particle size, sample weight, and sample packing. Experimental parameters that affect the DTA results include heating and cooling rate and the environment surrounding the sample. A reduction of heating rate involves more time per experiment. In general, the effect of lowering the heating rate is the same as that by lowering the sample weight. Employing a slow heating rate usually increases resolution, but reduces sensitivity. For a phase diagram measurement, a heating rate of 5 °C min^{-1} is usually adopted, since this heating rate appears to offer the best compromise between quality of resolution and time taken per experiment. However, in cases where an accurate phase transition temperature is required, such as a degenerated equilibrium, it may be necessary to investigate the effect of heating (and/or cooling) rate on the DTA trace [58]. Heating rates as low as 2 °C min^{-1} are not uncommon in this type of study. The atmosphere around the sample is another important factor that deserves attention. It may be either static or flowing, and may be either inert or reactive, depending on the compatibility with the process under investigation. For the determination of alloy phase diagrams, inert gas is usually chosen in order to avoid contamination, evaporation, and reaction with the environment such as oxidation. DTA is particularly useful for phase equilibria at higher temperatures (>1000 °C) or in aggressive environments, where heat-flux DSC instruments may not be able to operate.

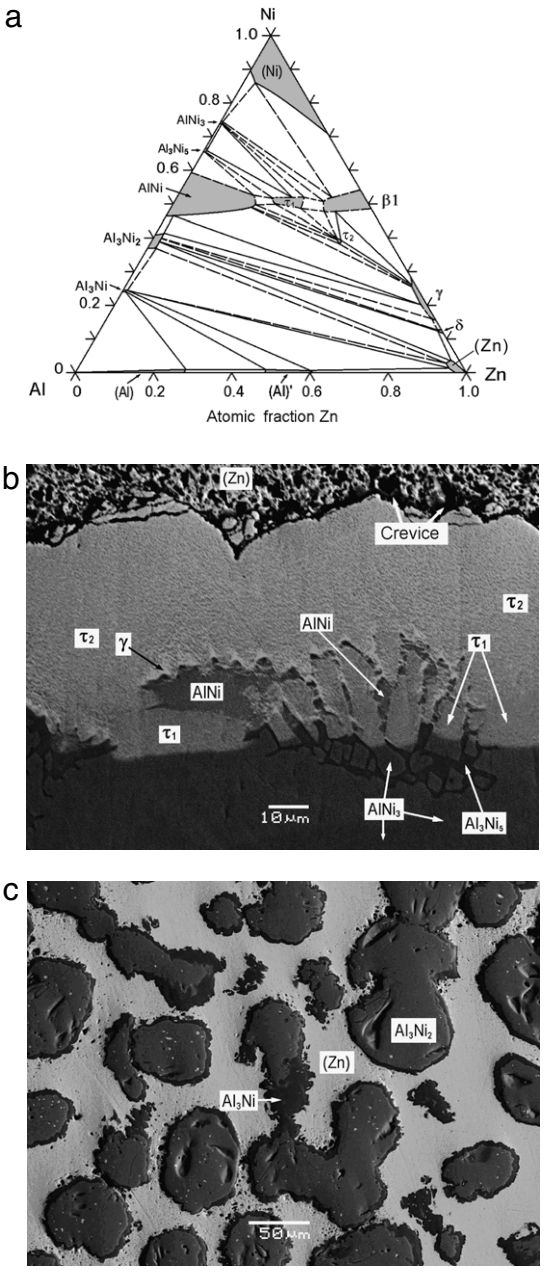

Fig. 3. (a) Experimental isothermal section at 340 °C of the Al–Ni–Zn system via a combination of diffusion couple and equilibrated alloys [50]. (b) BSE image of the $Al_{25}Ni_{75}$/Zn diffusion couples annealed at 340 °C for 380 h. (c) BSE image of the ternary alloy ($Al_{26}Ni_{13}Zn_{61}$) annealed at 340 °C for 480 h.

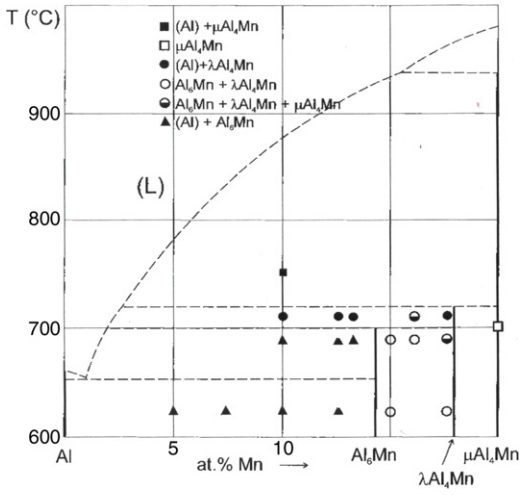

Fig. 4a. Phase relation in Al-rich side of the Al–Mn system derived from equilibration and quench experiments [31].

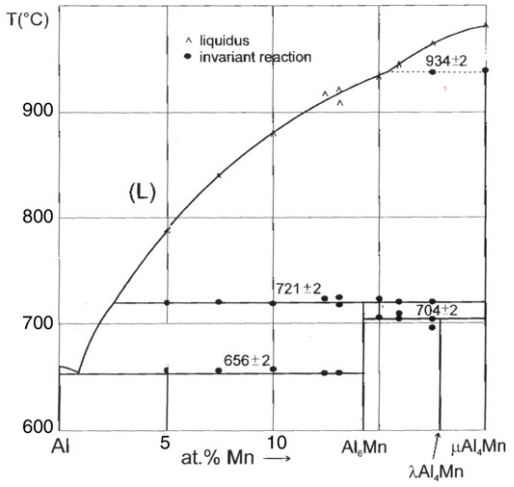

Fig. 4b. Phase relation in Al-rich side of the Al–Mn system derived from DTA measurement [31].

Although DTA is an effective approach to measure phase transition temperatures, it could yield erroneous results due to slow kinetics (such as nucleation barrier) of reactions during measurement [31]. Fig. 4a shows the phase relation in Al-rich side of the Al–Mn system derived from XRD analysis and microstructure observation of the equilibrated and quenched alloys. The DTA measurement of the same alloys yields the phase equilibrium as shown in Fig. 4b. As can be seen from Fig. 4, the phase relations resulting from each set of data contradict each other. XRD and microstructure observation indicate the existence of a phase field L+λ-$MnAl_4$, while the DTA data suggest no phase field L+λ-$MnAl_4$. Thus one of the experimental methods must yield misleading data. To resolve this discrepancy, a thorough analysis for the obtained data in view of phase identification, annealing, the formation of metastable phases, quenching, contamination, and the kinetics of the reactions is performed [31]. Among the above mentioned several possible reasons for the discrepancy, we found that the nucleation barrier for the formation of λ-$MnAl_4$ is responsible for the erroneous conclusions from data obtained with DTA technique. In order to investigate the kinetics associated with the formation of λ-$MnAl_4$, time-dependent annealing and quench experiments were performed for the alloy Al-12.5 at.% Mn annealed at 712 °C for 5, 50, 100, and 500 min, followed by water-quenching. XRD analysis shows no trace of λ-$MnAl_4$ was formed within the first 50 min and even after 500 min the transformation was not complete. At a heating rate of 5 K/min, it takes only 12 min to heat the alloy from 690 °C, where $MnAl_6$ is still found even after prolonged anneal, to 750 °C, where L + μ-$MnAl_4$ is observed to coexist. Reducing the heating rate to 2 K/min and assuming the unlikely case, that the phase field L + λ-$MnAl_4$ ranges from 690 °C to 750 °C, the phase λ–$MnAl_4$ has only 30 min to form or will not be detected by DTA. This evidence suggests that the formation of λ-$MnAl_4$ during incongruent of $MnAl_6$ is a slow nucleation controlled process. This nucleation barrier leads to the erroneous conclusions from data obtained by dynamic methods such as DTA technique. Care should be taken to check the general consistency of the phase diagram data obtained from different experimental methods.

Another issue, which should be taken into consideration when performing DTA measurement, is the capsule and the way how the capsule holder is installed. For most alloys, it is possible to use commercial DTA apparatuses to measure phase transition temperatures directly. In the case of the alloys with high oxygen affinity and vapor pressure, some modifications to the commercial DTA apparatus are needed since the reactive alloys would damage the DTA apparatus gradually during extensive measurements. Miller et al. [59] developed a welding apparatus which can be used to weld Ta, W and Mo as a container material for reactive or volative alloys, such as Mg alloys and rare-earth metals. Subsequently, Capelli et al. [60] developed a laboratory-made DTA using Ta or Mo as the container. This DTA apparatus has been used to measure many binary and ternary phase diagrams, which contain reactive or volatile elements such as La [61], Ce [62] and Mg [63]. Recently, Mirković and Schmid-Fetzer [64] developed a similar modification to the commercial DTA equipment using sealed Ta-capsules, as shown in Fig. 5. This adaptation was found to be indispensable for reproducible and reliable DTA experiments. In their modifications, the Ta-capsules were produced by using a Ta-tube with 10 mm outside diameter and 0.4 mm wall thickness and a Ta-sheet for the capsule lid and bottom with 0.25 mm thickness (Fig. 6). The Ta-capsules were filled up to 50 vol.% with the sample material and sealed by electric arc welding. The average empty Ta-capsule weight was 3520 mg, and the typical sample weight was about 400 mg [64].

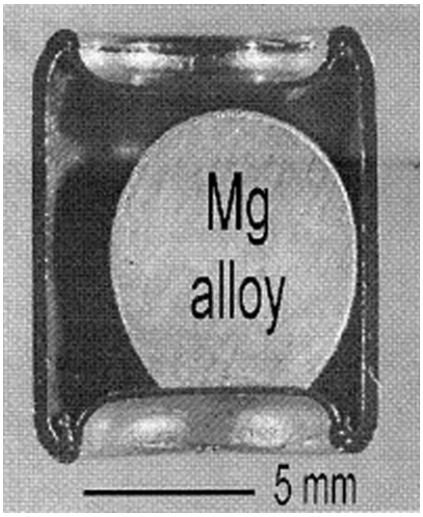

Fig. 5. Cross-section of the optimized Ta-capsule filled with Mg alloy after being measured with DTA [64].

2.4.2. DSC

DSC is a thermal analysis technique that measures the energy absorbed or emitted by a sample as a function of temperature

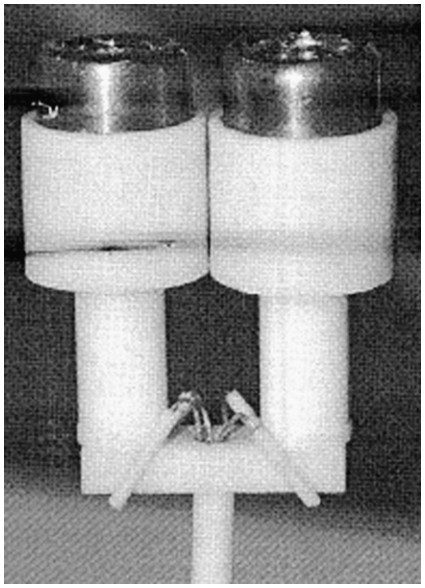

Fig. 6. Customized DTA sample holder with reference and sample capsule [64].

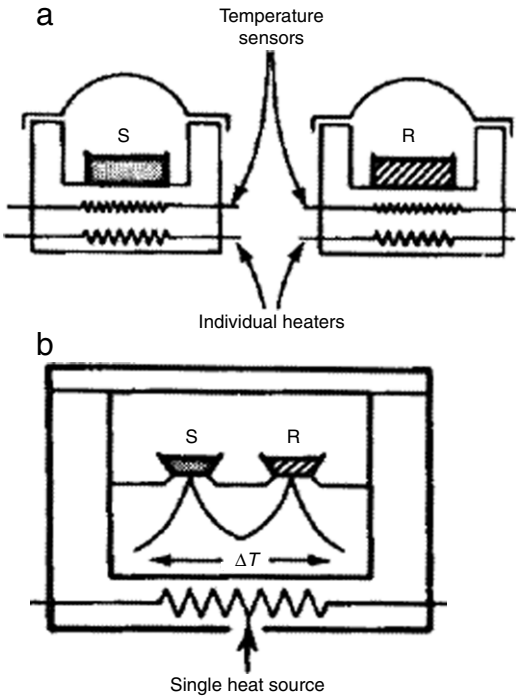

Fig. 7. Two types of DSC equipments: (a) Power-compensation DSC, and (b) heat-flux DSC. S = Sample, and R = Reference material.

or time. When a phase transition occurs, DSC provides a direct calorimetric measurement of the energy change at the transition temperature by subjecting the sample and an inert reference material to the identical temperature regime in an environment heated or cooled at a controlled rate. DSC equipment can be utilized not only to determine the liquidus line, solidus line and other phase transition points on a phase diagram, but also to measure some thermodynamic properties, such as enthalpy, entropy and specific heat, which are important for investigation of second-order phase transitions. One deficiency of DSC is that its usage temperature is usually in the range of −175 °C–1100 °C, much lower than that of DTA.

Two types of DSC apparatuses are in common usage: power-compensation DSC and heat-flux DSC. In the power-compensation DSC (Fig. 7 (a)), the temperatures of the sample and reference are controlled independently using separated but identical furnaces. The temperatures of the sample and the reference are made identical by varying the power input to the two furnaces. The energy required to do so is a measure of the enthalpy or heat capacity changes in the sample compared to the reference.

In the heat-flux DSC, the sample and reference are connected with a low-resistance heat-flow path (a metal disc). The assembly is enclosed in a single furnace, as illustrated in Fig. 7(b). Enthalpy or heat capacity changes in the sample cause a difference in its temperature relative to the reference. The resulting heat flow is smaller compared to that in DTA because the sample and the reference are in good thermal contact. The temperature difference is recorded, and such a difference is related to the enthalpy change of the sample during measurements.

Care is needed when using DSC to study a solid–solid phase transition where the enthalpy change is much smaller than that associated with melting or vaporization. The energy stored in the form of elastic strains and defects can contribute to the energy balance. This stored energy could reduce the observed enthalpy change.

2.5. Calorimetry

The widely used methods to measure thermodynamic properties [41] include, among others, calorimetric method, electromotive force (emf) technique, the isopiestic method, Torsion effusion method, and Knudsen effusion method. The quantities conveniently recorded for the thermodynamic description of inorganic and organic materials are the enthalpy of formation at 298 K, the standard entropy at 298 K, heat capacity, and the enthalpies of transformation or melting where applicable. Since all these data can in principle be obtained by means of suitable calorimeters, the calorimeter is generally regarded as the most important piece of equipment for a thermochemist. Kelppa and his colleagues have employed this method to measure enthalpies of formation for many important binary and ternary compounds [65,66]. Fig. 8 shows a schematic diagram of this calorimeter. It is worth mentioning that many authors, such as Predel and Sommer [67] Colinet [68] and Ferro [69], contributed to the building of calorimetric equipments used for the measurement of enthalpy of formation, heat capacity etc.

The fundamental of the calorimeter is described as follows with its application to the measurement of enthalpy of formation for ternary compounds in the Al–Fe–Ni system. Three stable ternary compounds, τ_1 (Al_9FeNi) and τ_2 ($Al_{10}Fe_3Ni$), and τ_3 ($Al_{71}Fe_5Ni_{24}$), exist in the Al–Fe–Ni system [29]. It is realized that the enthalpy of formation is the dominant term of Gibbs energy. However, the only measurement on the enthalpies of formation for the compounds in the Al–Fe–Ni system is from Su et al. [70], who determined the enthalpy of formation for τ_1 at room temperature ($\Delta H_f^{298\ K}$) by means of a reaction calorimetry. In order to provide more thermodynamic data for modeling, most recently we measured $\Delta H_f^{298\ K}$ for τ_2 using Kleppa-type high-temperature reaction calorimetry (HTRC).

The measurement of $\Delta H_f^{298\ K}$ for τ_2 phase was performed in the Kleppa-type HTRC with calorimeter temperature set at 1100 ± 2 °C. A protective argon atmosphere was used in the experiment. The calorimeter was calibrated using Cu before the measurement. Al (purity: 99.97 wt%), Fe (purity: 99.99 wt%), and Ni (purity: 99.996 wt%) elemental powders were used to synthesize the samples. To remove surface contamination, the Fe and Ni elemental powders were reduced in a hydrogen gas furnace immediately before preparing a compact of the elemental powders. 6 samples with the weight of about 100 mg and 1 sample about 120 mg were produced by mixing elemental powders in a mortar according to the required molar ratio for τ_2 phase, and

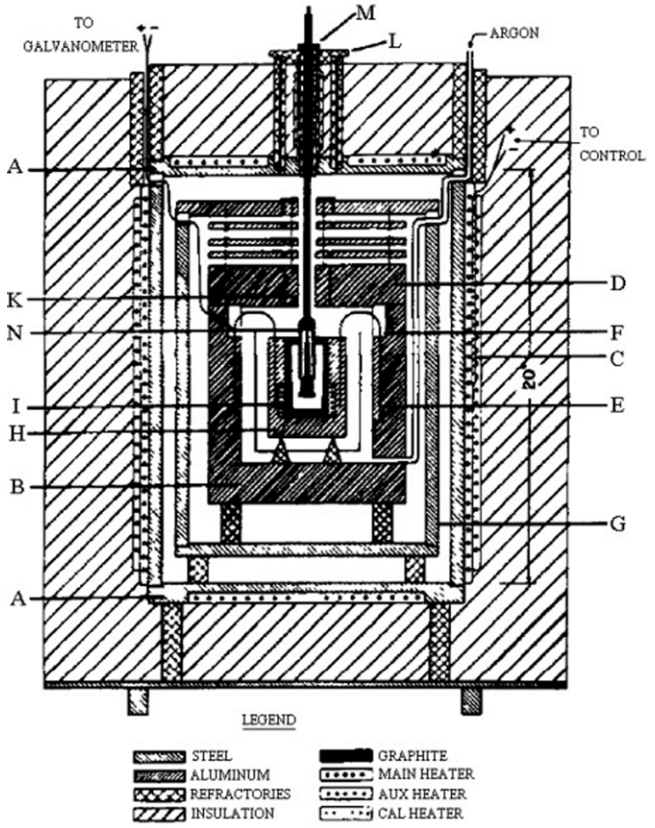

Fig. 8. Schematic diagram of the first high-temperature reaction calorimeter [65,66]. A = furnace core with main heaters, B = constant temperature jacket (aluminum), C = heavy shield (steel), D = calorimeter block (aluminum), E = calibration heater, F = removable crucible (graphite), G = charging or stirring device (graphite), H = inner plug, and I = out plug.

pressing them into small pellets. The enthalpy of formation was measured *via* two steps. In the first step, all the 7 samples were dropped into the calorimeter from room temperature, and then subsequently removed. The sample with the weight of about 120 mg was subject to XRD analysis to verify if the sample is in the single τ_2 phase after the high-temperature reaction synthesis. In the second step, the remaining 6 samples were again dropped from room temperature into the Kleppa-type calorimeter to obtain the heat content of this compound. The corresponding reactions associated with the above two steps are:

$$10 \cdot \mathrm{Al}(s, 25\ ^\circ\mathrm{C}) + 3 \cdot \mathrm{Fe}(s, 25\ ^\circ\mathrm{C}) + 1 \cdot \mathrm{Ni}(s, 25\ ^\circ\mathrm{C}) = \mathrm{Al_{10}Fe_3Ni}(1100\ ^\circ\mathrm{C}) \quad \Delta H_1 \tag{1}$$

$$\mathrm{Al_{10}Fe_3Ni}(s, 25\ ^\circ\mathrm{C}) = \mathrm{Al_{10}Fe_3Ni}(1100\ ^\circ\mathrm{C}) \quad \Delta H_2 \tag{2}$$

where s refers to the solid state, and ΔH_1 and ΔH_2 are the enthalpy changes for reactions 1 and 2, respectively. The difference between the two reactions yields the enthalpy of formation for τ_2 phase at room temperature:

$$\Delta H_{\mathrm{F}}^{298\ \mathrm{K}}(\mathrm{Al_{10}Fe_3Ni}) = \Delta H_1 - \Delta H_2. \tag{3}$$

The finally accepted $\Delta H_{\mathrm{f}}^{298\ \mathrm{K}}$ is the average of 6 individual measurements. With the standard deviations from the two steps designated as δ_1 and δ_2 and from the calibration as δ_3, the overall uncertainty δ in the $\Delta H_{\mathrm{f}}^{298\ \mathrm{K}}$ measurement was estimated to be $\delta = (\delta_1^2 + \delta_2^2 + \delta_3^2)^{1/2}$.

3. Computational approaches

Recently, attempts have been made to input the first-principles computed properties, such as structural energies, enthalpy of formation, elastic and magnetic properties, into the CALPHAD description of alloy systems [35]. The integration of first-principles calculation and CALPHAD modeling can provide fundamental information, which is usually not accessible experimentally, and thus can supplement the thermodynamic database. It is well established that first-principles method and related atomistic simulations can provide plentiful information on structural, thermodynamic, kinetic, mechanical, and other materials properties. In this section, we will briefly describe the fundamentals of first-principles calculation and CALPHAD approach, focusing on finite-temperature thermodynamic properties and the link between both approaches.

3.1. First-principles calculations

First-principles calculations based on DFT have enabled one to compute thermodynamic and structural properties of phases using only the atomic numbers and crystal structure information as input. It has been demonstrated by Wolverton et al. [36,37] and Liu et al. [39] that first-principles calculations provide a reliable way of predicting thermodynamic data when such data are not available in the literature. For alloys with high oxygen affinity and vapor pressure, it is extremely difficult to prepare alloys, which are suitable for experimental measurement of thermodynamic properties. In this case, first-principles calculations can be employed to provide these missing experimental data. If the phonon spectra can be obtained, the thermodynamic properties at finite temperatures can be obtained via the quasiharmonic approach [71]:

$$F_{Total}(V, T) = E_{0k}(V) + F_{vib}(V, T) + F_{el}(V, T) \tag{4}$$

where $E_{0k}(V)$ is the static energy or the 0 K energy. In this situation, the atoms are fixed at their static lattice positions. $F_{vib}(V, T)$ corresponds to the contribution from vibrational degrees of freedom to Gibbs free energy at series of volumes, and $F_{el}(V, T)$ is the contribution of thermally excited electrons to Gibbs energy.

$F_{vib}(V, T)$ can be calculated with the following equation:

$$F_{vib}(T) = k_{\mathrm{B}}T \int_0^\infty \ln\left[2\sin\left(\frac{h\upsilon}{2k_{\mathrm{B}}T}\right)\right] \cdot g(\upsilon)\mathrm{d}\upsilon \tag{5}$$

in which k_{B} is Boltzmann's constant, h Planck's constant, υ phonon frequency, T the temperature, and $g(\upsilon)$ the phonon density of state as a function of phonon frequency υ and volume V. For the sake of computational simplification, lattice vibrational effects are computed using either the supercell method or linear response theory within the harmonic approximation [38]. The harmonic approximation assumes small-amplitude atomic oscillations around equilibrium. The crystal potential can then be represented with a Taylor expansion of the real potential around the equilibrium positions of atoms. For detailed computational procedures, the reader is referred to the paper by Golumbfskie et al. [38], who computed the thermodynamic properties of the ternary compounds in the Al–Ni–Y system using the above method.

The electronic thermal contribution $F_{el}(V, T)$ in Eq. (4) is given by an equation of the form [72]:

$$F_{el} = E_{el} - TS_{el} \tag{6}$$

$$E_{el}(V, T) = \int_{-\infty}^{\infty} n(\varepsilon, V) f \varepsilon \mathrm{d}\varepsilon - \int_{-\infty}^{\varepsilon_F} n(\varepsilon, V)\varepsilon \mathrm{d}\varepsilon \tag{7}$$

$$S_{el}(V, T) = -k_{\mathrm{B}} \int n(\varepsilon, V)\,[f \ln f + (1-f) ln(1-f)]\,\mathrm{d}\varepsilon \tag{8}$$

$n(\varepsilon, V)$ is the electronic density of states (EDOS), and $f(\varepsilon, \mu, T_e)$ is the Fermi distribution function, which is defined as follows:

$$f(\varepsilon, \mu, T_e) = \frac{1}{\exp\left(\frac{\varepsilon-\mu}{k_{\mathrm{B}}T_e}\right) + 1} \tag{9}$$

in which μ is the electron chemical potential at T_e measured from the top of the valence band.

The heat capacity at constant volume (C_v) can be calculated via differentiating the Gibbs energy of lattice vibrations $F_{vib}(V, T)$, which reads:

$$C_v^{vib} = nk_B \int \left(\frac{\hbar\omega}{2k_BT}\right)^2 \cos ech^2\left(\frac{\hbar\omega}{2k_BT}\right) g(\omega)\, d\omega. \quad (10)$$

The heat capacity at constant pressure (C_p) is usually described with the following equation [73]:

$$C_p = C_v^{ele} + C_v^{vib} + \alpha^2 V_T BT \quad (11)$$

where α is the volume thermal expansion coefficient, B is the bulk modulus, and C_v^{ele} is the thermal electronic contribution to heat capacity, V_T is the variation of volume with temperature. According to Eq. (11), C_p is close to C_v^{vib} at low temperatures but larger than C_v^{vib} at high temperatures, where the thermal expansion effect is noticeable. Thus the key aspect to calculate C_p from first-principles calculations is to include the effects of thermal expansion on phonons. The quasiharmonic approximation is accounted by the harmonic approximation at several volumes in a specific temperature.

Since different first-principles methods, such as generalized gradient approximation (GGA) [74,75] and local density approximation (LDA) [76], might yield somewhat different results, it is recommended to employ different methods to compute the investigated properties. Such calculations can provide "the experimental error bar" if individual first-principles calculations are considered to be individual experiments. It is a common practice to use both the ultrasoft pseudopotential (USPP) method [77] and the projector augmented wave (PAW) method [78] to describe the electron–ion interaction. The exchange–correlation functional can be depicted by several different approaches, such as LDA [76], GGA-PW91 [74] and the GGA-PBE [75].

If the phonon spectra can be obtained, the above equations can be used to calculate the thermodynamic properties at finite temperatures for the phases.

When the calculated phonon spectra have imaginary frequencies or the calculations are computationally unaffordable due to the complex crystal structure, the Debye and related models [79] can be utilized to estimate the thermodynamic properties at finite temperatures with an accuracy below that from the first-principles calculations. According to these models, the Gibbs free energy can be expressed as follow:

$$G^*(V^*; P; T) = E(V) + PV + A_{vib}(\Theta(V)^*, T) + F_{el} \quad (12)$$

where $E(V)$ is the total energy per unit cell, PV corresponds to the constant hydrostatic pressure condition, $\Theta(V)$ is the Debye temperature, and A_{vib} is the vibrational term, which can be written as

$$A_{vib}\left(\Theta^*, T\right) = nk_BT\left[\frac{9\Theta}{8T} + 3\ln(1 - e^{-\Theta/T}) - D(\Theta/T)\right] \quad (13)$$

where n is the number of atoms per formula unit, $D(\Theta/T)$ represents the Debye integral. Θ is expressed as follows:

$$\Theta = \frac{\hbar}{k_B}\left[6\pi^2 V^{1/2} n\right]^{1/3} f(\sigma)\sqrt{\frac{B_S}{M}} \quad (14)$$

where M is the molecular mass per unit cell, B_s is the adiabatic bulk modulus and it is approximated by the static compressibility

$$\mathbf{B_S} \approx B(V) = V\left(\frac{d^2E(V)}{dV^2}\right). \quad (15)$$

The function $f(\sigma)$ is represented with the following expression:

$$f(\sigma) = \left\{\frac{1}{3}\left[2\left(\frac{2(1+\sigma)}{3(1-2\sigma)}\right)^{3/2} + \left(\frac{1+\sigma}{3(1-\sigma)}\right)^{3/2}\right]^{-1}\right\}^{1/3}. \quad (16)$$

And the Debye sound velocity V in Eq. (15) reads:

$$v_D = f(\sigma)\sqrt{\frac{B_s}{\rho}}. \quad (17)$$

The last term F_{el} in Eq. (12) is represented as follows:

$$F_{el} = -\frac{\pi^2}{6}N(E_F, V)(K_BT)^2 \quad (18)$$

where $N(E_F, V)$ is the electron density of states at the Fermi level E_F.

The cluster expansion (CE) method is a way of representing the energy of a configuration for an alloy on a lattice. This method can establish a link between the first-principles calculated internal energies of ordered structures and the internal energy for any other structure. In the present work, the energies of solid solution phases in the fcc-based alloy systems are derived within the first-principles cluster expansion framework. In this approach the internal energy is expressed in terms of a generalized Ising model in which the energy is expanded by means of a series of basic functions J_m, which are called the effective cluster interaction energies (ECIs). The ECIs are obtained by a fit to a set of cluster energies corresponding to many atomic configurations [80]. Then the cluster expansion parameterizes the energy of the alloy as follows:

$$E(V) = \sum_{m=0}^{m_{\max}} \xi_m J_m(V) \quad (19)$$

where m takes the value $0, \ldots, m_{\max}$ (in the case of the tetrahedron approximation $m_{\max}$ is equal to 4), ξ_m is the correlation function [81]. The value of ξ_m is associated with the cluster of the set of fcc-based compounds used in the present work. J_m (ECIs) can be extracted from the internal energies of a series of ordered compounds [82]. We can calculate J_m through the following matrix forms:

$$J_m = \xi^{-1} \times E_0 \quad (20)$$

where the ξ^{-1} is the inverse of the correlation function matrix ξ. E_0 is the energy matrix for a series of ordered structures.

The magnetic thermodynamics is still far from fully understood due to the occurrence of the phase transition at the Curie/Néel temperature. For a solid phase without phase transition, its thermodynamic property has been successfully depicted using the first-principles quasiharmonic approximation [83–85]. For magnetic thermodynamics, the magnetic contribution to Helmholtz energy is usually described by adding an extra term based on the Heisenberg model within the mean-field approximation (MFA) and the random phase approximation (RPA) [86]. But both MFA and RPA are only capable of predicting the heat capacity below Curie temperature T_C, incapable of depicting the region above T_C since both approximations do not capture the local magnetic order dominating in this region. The disordered local moment (DLM) model [87,88] can account for the possibility of random antiparallel spin alignments. Alling et al. [89] used the special quasirandom structure (SQS) [90] to mimic the paramagnetic (PM) CrN phase. However, only one SQS magnetic state was employed in the DLM model [89], implying its inability to describe the magnetic configurational entropy and in turn the anomalous magnetic properties. Recently, Wang et al. [91,92] proposed an alternative partition function approach (PFA) for first-principles magnetic thermodynamics. Such an approach is better than all the exist-

ing models. Within the framework of PFA, the magnetic thermodynamics can be resolved using thermodynamic fluctuations among the competing collinear magnetic configurations in accordance with the canonical partition function. While it should be pointed out that only the collinear magnetic states in PFA (ignoring other magnetic excitations such as the noncollinear, spin-wave, and magnon, etc.) are enough to account for the major magnetic thermodynamics containing anomalies.

3.2. CALPHAD modeling

With the experimentally measured phase diagram and thermodynamic data, supplemented with first-principles calculations, CALPHAD method can be used to optimize thermodynamic parameters of individual phases. By means of the powerful softwares, such as Thermo-calc [93], Pandat [94], FACT [95], and MTDATA [96], thermodynamic parameters for various thermodynamic models can be obtained via standard optimization procedures.

Thermodynamic modeling involving several disorder/order phase transformations for one phase represents a severe challenge for CALPHAD application to multicomponent alloys. Nowadays, it is of scientific interest to use a four-sublattice model $(A, B, C, \ldots)_{0.25}(A, B, C, \ldots)_{0.25}(A, B, C, \ldots)_{0.25}(A, B, C, \ldots)_{0.25}$ to describe fcc-based phases (disordered Fcc_A1, ordered $L1_2$, $L1_0$ and F′) and a four-sublattice model $(A, B, C, \ldots, Va)_{0.25}(A, B, C, \ldots, Va)_{0.25}(A, B, C, \ldots, Va)_{0.25}(A, B, C, \ldots, Va)_{0.25}$ to describe bcc-based phases (disordered Bcc_A2, ordered Bcc_B2, DO_3 and B32) in which A, B, and C are the elements, and Va is the vacancy. To the best of our knowledge, so far a four-sublattice model has probably applied to a few binary and ternary systems, such as the Al–Ni [97], Al–Fe [98], Al–Cr–Ni [97], Al–Ni–Pt [99], and Fe–Ni–Ti [100] systems. In the literature, many binary systems are described with a two-sublattice model for disordered and ordered phases. It is a tremendous amount of work to use a four-sublattice model to remodel those binary systems in which there are several disorder/order phase transformations for one phase.

As mentioned above, it is of scientific interest to use a 4SL model to describe order/disorder transitions nowadays. That is because 4SL model can describe disordered Fcc_A1, and ordered $L1_2$ and $L1_0$ phases simultaneously, while 2SL model can only describe the Fcc_A1 and $L1_2$ phases. Though 4SL has the noticeable superiority, however, the present situation is that most of the available binary and ternary systems are described with a 2SL model in the literature. Such a situation may be due to the two major points: (i) high requirements on the software for calculating phase equilibria with 4SL models, which have been usually avoided in the literature, and (ii) only stable $L1_2$ phase exits in most systems while $L1_0$ phase not. Therefore, it could be a compromise to accept the existing 2SL models for most systems, and convert the parameters of 4SL model into those of 2SL one in order to keep the consistency of the database.

It should be noted that only the conversion from 4SL into 2SL is mentioned here, but not the full conversion between 2SL and 4SL. That is because the ordered energy in 4SL model includes the $L1_2$ and the $L1_0$ branches. When we convert 4SL model into 2SL, it is assumed that the three sublattices in 4SL are equivalent, while the fourth one is different. In this case, only 2SL branch is converted. Another important thing is that 2SL branch also inherits the lattice stabilities of the elements and the set of mixing parameters from the disordered phase at the same time, as shown in Eq. (21). It means that a similar treatment of the $L1_0$ branch is no longer possible since the $L1_2$ ordering scheme is now linked to the disordered fcc phase. As for the conversion from 2SL to 4SL, it should be almost impossible from the practical point of view because the parameters in 2SL are based on the $L1_2$ information, but without $L1_0$. Moreover, $L1_0$ phase is metastable in most cases, and there is seldom experimental information.

In 2SL model, $L1_0$ ordering branch has been described by a formally separated phase with a symmetrical constitutional model $(A, B, C)_{0.5}(A, B, C)_{0.5}$, since the $L1_2$ ordering branch has been linked to the Fcc_A1 phase. In the systems where the $L1_0$ is stable and the 4SL model is available, we have performed the conversion in order to keep the representation of the $L1_0$ is equivalent to the respective branch of the 4SL model in all aspects [101]. For the bcc-based ordered structures, due to lack of experimental data, only ordered Bcc_B2 has been considered in the present database.

Since many binary systems in the literature have been modeled with a two-sublattice model for order/disorder phase transformation, a program to establish a thermodynamic database for the Al–Cu–Fe–Mg–Mn–Ni–Si–Zn system is in progress in our group by accepting the descriptions for these binary systems. In the following, we will demonstrate the integration of CALPHAD modeling and first-principles calculation through the expression for Gibbs energies of Fcc_A1 and $L1_2$ phases in the Al–Fe–Ni system [29]. It is noted that most recently the Al–Fe system has been reassessed with a four-sublattice model for the descriptions of disordered Bcc_A2, ordered Bcc_B2, DO_3 and B32 phases [98]. Thus it is of interest to update our previous description [29] for the Al–Fe–Ni system by using four-sublattice models to describe the various forms of bcc- and fcc-based disordered/ordered phases. Nevertheless, our previous description for the Al–Fe–Ni system [29] is briefly summarized in order to demonstrate the importance for the integration of CALPHAD approach and first-principles calculations.

In the Al–Fe–Ni system, the ordered ternary $L1_2$ phase is modeled as $(Al, Fe, Ni)_{0.75}(Al, Fe, Ni)_{0.25}$. To represent the Gibbs energies of both ordered $L1_2$ and disordered Fcc_A1 phases using a single function, the ternary Fcc_A1 is described by a model (Al, Fe, Ni). Consequently, the Gibbs energy of both $L1_2$ and Fcc_A1 is given by an equation of the form:

$$G_m^{L1_2,Fcc\_A1} = G_m^{Fcc\_A1}(x_{Al}, x_{Fe}, x_{Ni}) + G_m^{L1_2}(y'_{Al}, y'_{Fe}, y'_{Ni}, y''_{Al}, y''_{Fe}, y''_{Ni}) - G_m^{L1_2}(x_{Al}, x_{Fe}, x_{Ni}) \quad (21)$$

where y'_{Al}, y'_{Fe} and y'_{Ni} are the site fractions of Al, Fe and Ni in the first sublattice, and y''_{Al}, y''_{Fe} and y''_{Ni} in the second one. $G_m^{Fcc\_A1}(x_{Al}, x_{Fe}, x_{Ni})$ is the Gibbs energy of the disordered Fcc_A1 phase. The second term, $G_m^{L1_2}(y'_{Al}, y'_{Fe}, y'_{Ni}, y''_{Al}, y''_{Fe}, y''_{Ni})$, is described by the sublattice model and implicitly contains a contribution from the disordered state. The last term, $G_m^{L1_2}(x_{Al}, x_{Fe}, x_{Ni})$, represents that contribution from the disordered state to the ordered one. When the site fractions are equal, *i.e.* $y'_{Al} = y''_{Al}$, $y'_{Fe} = y''_{Fe}$, and $y'_{Ni} = y''_{Ni}$, the last two terms cancel each other. In this case, Eq. (21) corresponds to the disordered state. The Gibbs energy of Fcc_A1 is described by Redlich–Kister polynomial.

According to the mathematical equivalence between the two-sublattice model (2SL) and the four-sublattice model (4SL), Ansara et al. [97,102] derived the following relations for the Gibbs energies of binary and ternary $L1_2$ phase under the assumption of the crystallographic equivalence of 4SL:

$${}^{2SL}G^{L1_2}_{B:A} = {}^{4SL}G^{L1_2}_{AB_3} \quad (22)$$

$${}^{2SL}G^{L1_2}_{A:B} = {}^{4SL}G^{L1_2}_{A_3B} \quad (23)$$

$${}^{2SL}L^{L1_2,0}_{A,B:A} = -\frac{3}{2}{}^{4SL}G^{L1_2}_{AB_3} + \frac{3}{2}{}^{4SL}G^{L1_2}_{A_2B_2} + \frac{3}{2}{}^{4SL}G^{L1_2}_{A_3B} \quad (24)$$

$${}^{2SL}L^{L1_2,0}_{A,B:B} = +\frac{3}{2}{}^{4SL}G^{L1_2}_{AB_3} + \frac{3}{2}{}^{4SL}G^{L1_2}_{A_2B_2} - \frac{3}{2}{}^{4SL}G^{L1_2}_{A_3B} \quad (25)$$

$${}^{2SL}L^{L1_2,1}_{A,B:A} = +\frac{1}{2}{}^{4SL}G^{L1_2}_{AB_3} - \frac{3}{2}{}^{4SL}G^{L1_2}_{A_2B_2} + \frac{3}{2}{}^{4SL}G^{L1_2}_{A_3B} \quad (26)$$

$$^{2SL}L^{L1_2,1}_{A,B:B} = +\frac{3}{2}{}^{4SL}G^{L1_2}_{AB_3} + \frac{3}{2}{}^{4SL}G^{L1_2}_{A_2B_2} - \frac{1}{2}{}^{4SL}G^{L1_2}_{A_3B} \quad (27)$$

$$^{2SL}L^{L1_2,0}_{*:A,B} = {}^{4SL}L^{L1_2,0}_{A,B} \quad (28)$$

$$^{2SL}L^{L1_2,1}_{*:A,B} = {}^{4SL}L^{L1_2,1}_{A,B} \quad (29)$$

$$^{2SL}L^{L1_2,0}_{A,B:*} = 3^{4SL}L^{L1_2,0}_{A,B} \quad (30)$$

$$^{2SL}L^{L1_2,1}_{A,B:*} = 3^{4SL}L^{L1_2,1}_{A,B} \quad (31)$$

$$^{2SL}L^{L1_2,0}_{A,B:C} = -\frac{3}{2}{}^{4SL}G^{L1_2}_{A_3C} - \frac{3}{2}{}^{4SL}G^{L1_2}_{B_3C} + \frac{3}{2}{}^{4SL}G^{L1_2}_{AB_2C} + \frac{3}{2}{}^{4SL}G^{L1_2}_{A_2BC} \quad (32)$$

$$^{2SL}L^{L1_2,0}_{A,C:B} = -\frac{3}{2}{}^{4SL}G^{L1_2}_{A_3B} - \frac{3}{2}{}^{4SL}G^{L1_2}_{BC_3} + \frac{3}{2}{}^{4SL}G^{L1_2}_{ABC_2} + \frac{3}{2}{}^{4SL}G^{L1_2}_{A_2BC} \quad (33)$$

$$^{2SL}L^{L1_2,0}_{B,C:A} = -\frac{3}{2}{}^{4SL}G^{L1_2}_{AB_3} - \frac{3}{2}{}^{4SL}G^{L1_2}_{AC_3} + \frac{3}{2}{}^{4SL}G^{L1_2}_{ABC_2} + \frac{3}{2}{}^{4SL}G^{L1_2}_{AB_2C} \quad (34)$$

$$^{2SL}L^{L1_2,1}_{A,B:C} = -\frac{1}{2}{}^{4SL}G^{L1_2}_{A_3C} + \frac{1}{2}{}^{4SL}G^{L1_2}_{B_3C} - \frac{3}{2}{}^{4SL}G^{L1_2}_{AB_2C} + \frac{3}{2}{}^{4SL}G^{L1_2}_{A_2BC} \quad (35)$$

$$^{2SL}L^{L1_2,1}_{A,C:B} = -\frac{1}{2}{}^{4SL}G^{L1_2}_{A_3B} + \frac{1}{2}{}^{4SL}G^{L1_2}_{BC_3} - \frac{3}{2}{}^{4SL}G^{L1_2}_{ABC_2} + \frac{3}{2}{}^{4SL}G^{L1_2}_{A_2BC} \quad (36)$$

$$^{2SL}L^{L1_2,1}_{B,C:A} = -\frac{1}{2}{}^{4SL}G^{L1_2}_{AB_3} + \frac{1}{2}{}^{4SL}G^{L1_2}_{AC_3} - \frac{3}{2}{}^{4SL}G^{L1_2}_{ABC_2} + \frac{3}{2}{}^{4SL}G^{L1_2}_{AB_2C} \quad (37)$$

$$^{2SL}L^{L1_2,0}_{A,B,C:A} = +{}^{4SL}G^{L1_2}_{AB_3} - \frac{3}{2}{}^{4SL}G^{L1_2}_{A_2B_2} - \frac{3}{2}{}^{4SL}G^{L1_2}_{A_3B} + {}^{4SL}G^{L1_2}_{AC_3} - \frac{3}{2}{}^{4SL}G^{L1_2}_{A_2C_2} - \frac{3}{2}{}^{4SL}G^{L1_2}_{A_3C} - \frac{3}{2}{}^{4SL}G^{L1_2}_{ABC_2} - \frac{3}{2}{}^{4SL}G^{L1_2}_{AB_2C} + 6^{4SL}G^{L1_2}_{A_2BC} \quad (38)$$

$$^{2SL}L^{L1_2,0}_{A,B,C:B} = -{}^{4SL}G^{L1_2}_{AB_3} - \frac{3}{2}{}^{4SL}G^{L1_2}_{A_2B_2} + {}^{4SL}G^{L1_2}_{A_3B} + {}^{4SL}G^{L1_2}_{BC_3} - \frac{3}{2}{}^{4SL}G^{L1_2}_{B_2C_2} - \frac{3}{2}{}^{4SL}G^{L1_2}_{B_3C} - \frac{3}{2}{}^{4SL}G^{L1_2}_{ABC_2} + 6^{4SL}G^{L1_2}_{AB_2C} - \frac{3}{2}{}^{4SL}G^{L1_2}_{A_2BC} \quad (39)$$

$$^{2SL}L^{L1_2,0}_{A,B,C:C} = -\frac{3}{2}{}^{4SL}G^{L1_2}_{AC_3} - \frac{3}{2}{}^{4SL}G^{L1_2}_{A_2C_2} + {}^{4SL}G^{L1_2}_{A_3C} - \frac{3}{2}{}^{4SL}G^{L1_2}_{BC_3} - \frac{3}{2}{}^{4SL}G^{L1_2}_{B_2C_2} + {}^{4SL}G^{L1_2}_{B_3C} + 6^{4SL}G^{L1_2}_{ABC_2} - \frac{3}{2}{}^{4SL}G^{L1_2}_{AB_2C} - \frac{3}{2}{}^{4SL}G^{L1_2}_{A_2BC} \quad (40)$$

where the asterisk (*) means that the interaction parameters are independent of the atom occupation in the * indicated sublattice. The parameters with superscript 2SL and 4SL mean the parameters resulting from two- and four-sublattice, respectively. The above relations can be simplified when the Gibbs energy of each stoichiometric compound is defined as:

$$^{4SL}G^{L1_2}_{A:B:C:D} = U_{AB} + U_{AC} + U_{AD} + U_{BC} + U_{BD} + U_{CD} + \alpha_{ABCD} \quad (41)$$

in which U_{AB}, U_{AC}, U_{AD}, U_{BC}, U_{BD} and U_{CD} are parameters related to bonding energy between A–B, A–C, A–D, B–C, B–D and C–D atoms, while α_{ABCD} is one adjustable parameter during thermodynamic assessment, indicating that $^{4SL}G^{L1_2}_{A:B:C:D}$ is also adjustable in order to fit the experimental data. In a binary system, α_{ABCD} is usually set to zero. Eqs. (22)–(40) can be simplified substantially by using Eq. (41).

However, some modifications were made for fcc_A1/$L1_2$ order/disorder transition. Eqs. (22)–(40) derived by Ansara et al. [97,102] were not used in the Al–Fe–Ni system due to $^{4SL}G^{L1_2}_{FeNi_3} \neq {}^{4SL}G^{L1_2}_{Fe_3Ni}$ in the binary Fe–Ni system, making it impossible to estimate $^{4SL}G^{L1_2}_{AlFeNi_2}$, $^{4SL}G^{L1_2}_{AlFe_2Ni}$ and $^{4SL}G^{L1_2}_{Al_2FeNi}$ in the ternary Al–Fe–Ni system *via* Eq. (41). This problem can be solved in two alternative ways. One is to optimize $^{4SL}G^{L1_2}_{AlFeNi_2}$, $^{4SL}G^{L1_2}_{AlFe_2Ni}$ and $^{4SL}G^{L1_2}_{Al_2FeNi}$ based on the experimental data associated with the $L1_2$ phase, and the other is to directly obtain these values using first-principles calculations. Considering the fact that there is a large amount of experimental data relevant to the $L1_2$ phase in the Al–Fe–Ni system and the first-principles calculations will lead to burdensome tasks because there are so many ternary, quaternary, and even higher order systems related to the Fe–Ni system in a multicomponent alloy database, the simplification proposed by Zhang et al. [103], $U_{FeNi} = \frac{1}{3}{}^{4SL}G^{L1_2}_{FeNi_3}$, are utilized in the Al–Fe–Ni system. Then, the following expressions can be derived according to Refs. [97,102,103]:

$$^{4SL}G^{L1_2}_{Al_2FeNi} = \frac{2}{3}\cdot{}^{4SL}G^{L1_2}_{Al_3Fe} + \frac{2}{3}\cdot{}^{4SL}G^{L1_2}_{Al_3Ni} + \frac{1}{3}\cdot{}^{4SL}G^{L1_2}_{Ni_3Fe} + \alpha_{Al_2FeNi} \quad (42)$$

$$^{4SL}G^{L1_2}_{AlFe_2Ni} = \frac{2}{3}\cdot{}^{4SL}G^{L1_2}_{Al_3Fe} + \frac{1}{3}\cdot{}^{4SL}G^{L1_2}_{Al_3Ni} + \frac{2}{3}\cdot{}^{4SL}G^{L1_2}_{Ni_3Fe} + \alpha_{AlFe_2Ni} \quad (43)$$

$$^{4SL}G^{L1_2}_{AlFeNi_2} = \frac{1}{3}\cdot{}^{4SL}G^{L1_2}_{Al_3Fe} + \frac{2}{3}\cdot{}^{4SL}G^{L1_2}_{Al_3Ni} + \frac{2}{3}\cdot{}^{4SL}G^{L1_2}_{Ni_3Fe} + \alpha_{AlFeNi_2} \quad (44)$$

where α_{Al_2FeNi}, α_{AlFe_2Ni} and α_{AlFeNi_2} are adjustable parameters. In order to check the reliability of the optimized parameters for $L1_2$ phase, first-principles calculations were also employed to calculate the enthalpies of formation for Al_2FeNi, $AlFe_2Ni$ and $AlFeNi_2$ in the ordered $L1_2$ structure at 0 K. These first-principles calculations can reduce the number of adjustable parameters in thermodynamic modeling and provide good starting values for some of thermodynamic parameters to be optimized.

4. Thermodynamic description of the Al–Fe–Ni system: a case study

Perhaps the Al–Fe–Ni ternary system is one of the most important ternary systems reported in the literature since this ternary system is the key ternary system in Al-, Fe-, and Ni-based alloys. The major contributions to the establishment of the phase equilibria in the Al–Fe–Ni system are due to Chumak et al. [104–106] and Zhang et al. [107,108]. Three stable ternary compounds (τ_1, τ_2 and τ_3) in the Al–Fe–Ni system are reported in the literature.

Using XRD, EPMA and DTA, Chumak et al. [104–106] measured the complete isothermal section at 850 °C, the partial isothermal sections at 1200, 1100, 1000 and 900 °C close to the Fe–Ni side, a series of vertical sections and invariant reactions in the Al-rich region.

In order to provide a thermodynamic description for the Al–Fe–Ni system over the whole composition and temperature ranges, we employed a hybrid approach of key experiment,

first-principles calculations and CALPHAD method. It is expected that this hybrid approach is equally applicable to other ternary systems. In the following we will demonstrate how we obtained a thermodynamic description for the whole Al–Fe–Ni system using the hybrid approach [29].

By means of a combination of XRD, SEM/EDX, EPMA and DTA, first we [107,108] measured the isothermal sections at 850 and 627 °C and determined the phase transition temperatures in the Al-rich region in order to provide decisive missing phase diagram data. Second, the enthalpy of formation for the representative ternary compound τ_2 was determined via a combination of a high-temperature reaction calorimeter and first-principles calculations. The finite-temperature thermodynamic properties due to vibrational degrees of freedom were calculated using the supercell method within the harmonic approximation. The first-principles calculations were also performed to compute the enthalpies of formation for the end members in the sublattice models of τ_1 and τ_2 as well as those of Al_2FeNi, $AlFe_2Ni$ and $AlFeNi_2$ in ordered $L1_2$ structure at 0 K. These calculations are used to reduce the number of adjustable parameters in thermodynamic modeling and provide reliable thermodynamic quantities for metastable phases. Finally based on the reliable literature data and our own experimental data including the first-principles generated data, a self-consistent set of thermodynamic parameters for the entire Al–Fe–Ni system can be obtained via CALPHAD method. Fig. 9 presents the calculated thermodynamic properties of τ_1 and τ_2 at finite temperatures via first-principle calculations. The calculated isothermal section at 850 °C is presented in Fig. 10. Fig. 11 shows the calculated activities of Fe and Ni at 1200 °C in γ' single-phase and $\gamma' + \beta$ two-phase regions along the vertical section of $x_{Ni}/x_{Al} = 3$ in comparison with the corresponding experimental data [109]. Figs. 12 and 13 present the calculated liquidus projection and reaction scheme for the entire Al–Fe–Ni system, respectively.

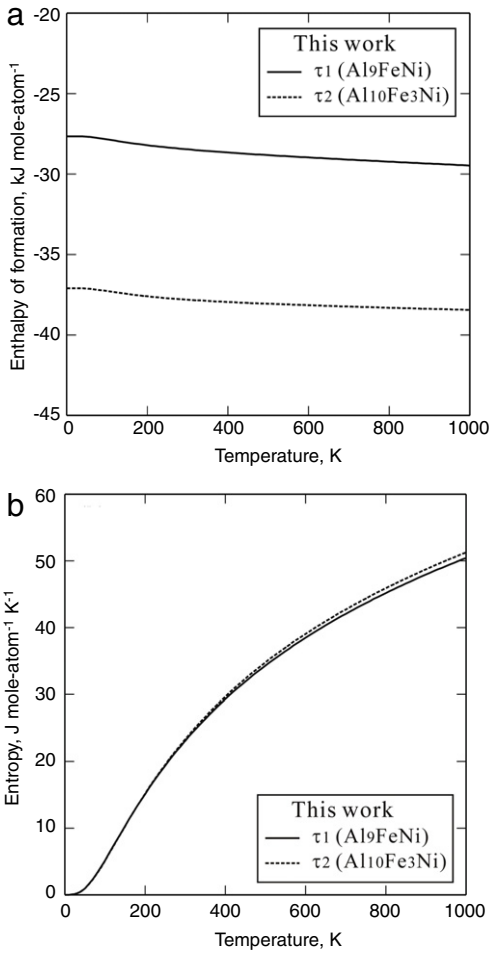

Fig. 9. Calculated thermodynamic properties of τ_1 and τ_2 phases in the Al–Fe–Ni system at finite temperatures *via* first-principle calculations [29]: (a) Enthalpies of formation for τ_1 and τ_2 phases; and (b) entropies for τ_1 and τ_2 phases. Lattice vibration effects were calculated using the supercell method within the harmonic approximations.

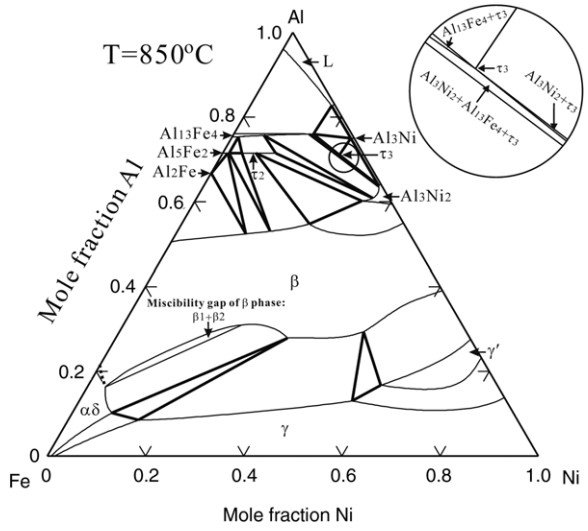

Fig. 10. Calculated isothermal section at 850 °C [29]. The dotted line denotes the order/disorder A2/B2 transition.

5. Brief summary for the thermodynamic modeling of the Al–Cu–Fe–Mg–Mn–Ni–Si–Zn system: focusing on the Al–Fe–Mg–Mn–Si quinary system

There are 28 binary systems in the Al–Cu–Fe–Mg–Mn–Ni–Si–Zn system. We have reassessed the Al–Mn [31], Cu–Mn [110], Cu–Zn [111], Mn–Ni [101], Fe–Zn [112], and Ni–Zn [113] binary systems since previous descriptions for the above six binary systems are of less physical meaning or the thermodynamic models in these binary systems are not compatible with the thermodynamic descriptions reported in the literature for the remaining binary systems of the Al–Cu–Fe–Mg–Mn–Ni–Si–Zn system. Fig. 14 presents the updated phase diagrams [31,110,111, 101,112,113] for the above six binary systems. The thermodynamic descriptions reported in the literature are adopted for the Al–Mg [114], Al–Ni [97], Cu–Si [115], Fe–Ni [116], Mg–Mn [117], Mg–Ni [118], Mg–Si [119], Mn–Zn [120], and Ni–Si [121]. And the descriptions for the remaining binary systems are taken from COST 507 [21].

With the above developed thermodynamic descriptions for the binary systems, thermodynamic modeling for the ternary systems can be performed with key experiments. First-principles calculations can be employed to provide missing experimental data, reduce the number of adjustable parameters and provide good starting values for thermodynamic parameters to be optimized, as demonstrated in the case study for the Al–Fe–Ni system. Following the similar approach as that employed for the Al–Fe–Ni system [29], we have investigated some important ternary systems in Al alloys, such as Al–Mn–Si [19], Al–Fe–Si [28], Al–Mg–Mn [31], Al–Cu–Si [122], Al–Cu–Ni [123], Al–Cu–Fe [124], and Al–Ni–Si [30] systems.

In the following, our recent work on the thermodynamic modeling of the Al–Fe–Mg–Mn–Si quinary system is presented. In order to describe this quinary system thermodynamically, the

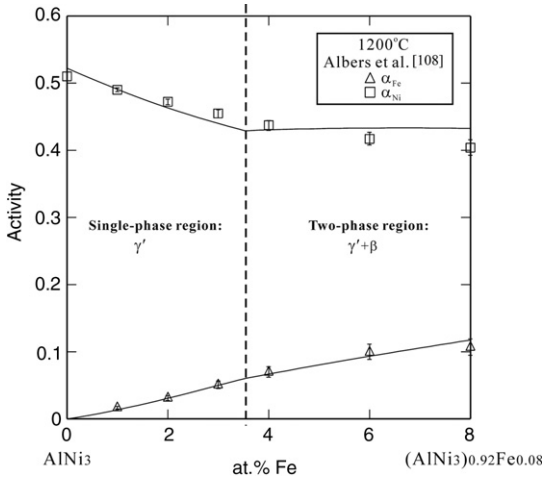

Fig. 11. Calculated activities of Fe and Ni at 1200 °C in $\gamma\prime$ single-phase and $\gamma + \beta$ two-phase regions along $x_{Ni}/x_{Al} = 3$ [29], compared with the corresponding experimental data [109]. The calculated activities in the two-phase region are not horizontal since the alloy compositions are not on tie lines along this vertical section.

quaternary systems should be first modeled. The thermodynamic descriptions of the ternary systems in this quinary system are from Al–Fe–Mg [101], Al–Fe–Mn [125], Al–Fe–Si [28], Al–Mg–Mn [31], Al–Mg–Si [21], Al–Mn–Si [19], Fe–Mg–Mn [126], Fe–Mg–Si [127], Fe–Mn–Si [128], and Mg–Mn–Si [129].

5.1. Al–Fe–Mg–Mn

No quaternary phases were found in the Al–Fe–Mg–Mn quaternary system [15]. The thermodynamic properties for the system are synthesized from the descriptions of the constituent ternary systems. Table 1 shows the comparison between the calculated invariant equilibria and the experimental data [130], which indicates a reasonable fit to the experimental data.

5.2. Al–Fe–Mg–Si

Using TA and OM, Phillips [6] investigated the phase equilibria in the Al-rich side of the Al–Fe–Mg–Si system in the composition ranges of 0–12 wt% Mg, 0–14 wt% Si, and 0–2.5 wt% Fe. On the basis of TA and chemical analysis, Gul'din and Dokukina [131] measured the solubilities of Fe and Si in Al–Mg melts and the eutectic reaction temperature for the reaction L = (Al) + Mg_2Si + $Al_{13}Fe_4$ + Al_8Mg_5.

The quaternary phase π ($Al_{16}Fe_2Mg_6Si_{12}$) found by Phillips [6] was shown to have the composition $Al_{18}Fe_2Mg_7Si_{10}$ by Krendelsberger et al. [132] using single crystal automatic four circle counter data. This quaternary phase π is treated as a stoichiometric phase, and its Gibbs energy is expressed relative to the mechanical mixing of the pure elements by the following equation:

$$G_m^{Al_{18}Fe_2Mg_7Si_{10}} - H^{SER} = 18 \cdot {}^{\circ}G_{Al}^{fcc-Al} + 2{}^{\circ}G_{Fe}^{bcc-A2} + 7{}^{\circ}G_{Mn}^{cbcc-A12} + 10 \cdot {}^{\circ}G_{Si}^{dia.} + A + BT \quad (45)$$

in which the coefficients A and B are assessed from the experimental phase diagram data.

In the present work, the Gibbs energy of formation for the quaternary phase $Al_{18}Fe_2Mg_7Si_{10}$ relative to its constituent elements is optimized to be −11 592 J/(mol-atoms) by using the measured invariant phase equilibria [6,131]. The calculated phase equilibria agree reasonably with the experimental data [6,131], as shown in Table 2, Fig. 15.

5.3. Al–Fe–Mn–Si

The phase equilibria in the Al-rich side of the quaternary Al–Fe–Mn–Si system have been the subject of numerous investigations [5,15,23,133–139]. By means of TA and metallographic examination methods, Phillips and Varley [5] obtained the liquidus surface, the solidus surface, and 16 isopleths over the composition ranges of 0–4 wt% Fe, 0–4 wt% Mn, and 0–4 wt% Si. They found the existence of the ternary phases α-AlFeSi(Al_8Fe_2Si), β-AlFeSi(Al_5FeSi), and α-AlMnSi($Al_{15}Mn_3Si_2$). α-AlMnSi and α-AlFeSi form a continuous series of solid solution [5]. Employing XRD and metallographic observation techniques, Nowotny and Marquardt [133] measured the 500 °C isothermal section of the Al–Fe–Mn–Si system at 88 wt% Al and below 12 wt% Fe and 12 wt% Mn. The isothermal section presented by them [133] is based on imperfect ternaries and is, therefore, of limited value. Phragmen [15] found a quaternary phase with the composition α-Al(Fe, Mn)Si. The existence of this quaternary phase was confirmed by Barlock and Mondolfo [130], who suggested the stoichiometry $Al_{15}(Fe, Mn)_3Si_2$ using XRD technique.

The six vertical sections below 4 wt% Mn were constructed by Zakharov et al. [23,134] using DTA, OM, and XRD techniques. In the presented sections, the phase boundaries are based on the cooling

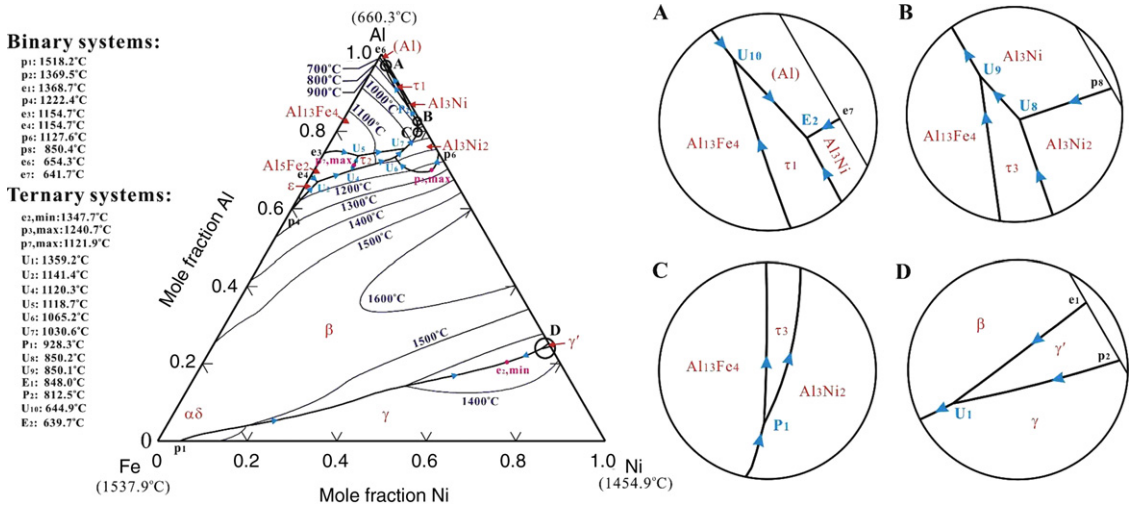

Fig. 12. Calculated liquidus projection of the entire Al–Fe–Ni system [29].

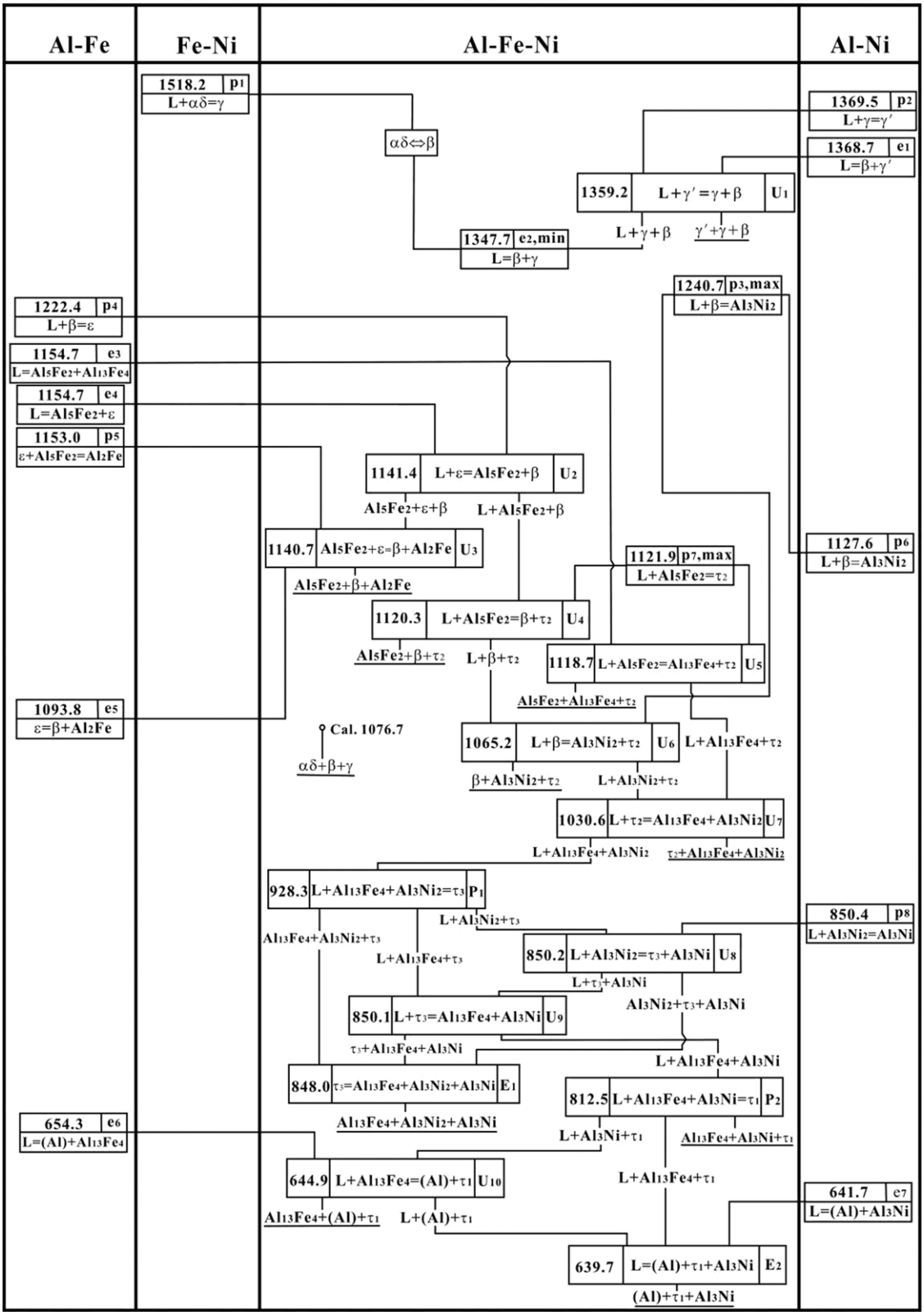

Fig. 13. Reaction scheme for the entire Al–Fe–Ni system [29]. Temperature is in °C.

curves with cooling rates of 2–3 K min^{-1}. In addition to the vertical sections, Zakharov et al. [23,134] reported the existence of a quaternary phase with a stoichiometry $Al_{16}(Fe, Mn)_4Si_3$. They also found that either α-AlFeSi or β-AlFeSi and α-AlMnSi do not form continuous solid solutions owing to the different crystal structures. It was reported that β-AlFeSi and α-AlMnSi dissolve less than 0.5 at.% Mn and less than 1 at.% Fe, respectively. Thoresen et al. [135] and Simensen et al. [136,137] confirmed that α-AlFeSi dissolves a small amount of Mn (up to 0.5 at.%). Using DTA technique, Flores-Valdes et al. [138] reported that the melting temperature corresponding to the stoichiometry $Al_8FeMnSi_2$ is 795 °C. It is not clear if the quaternary phase is formed congruently or via a

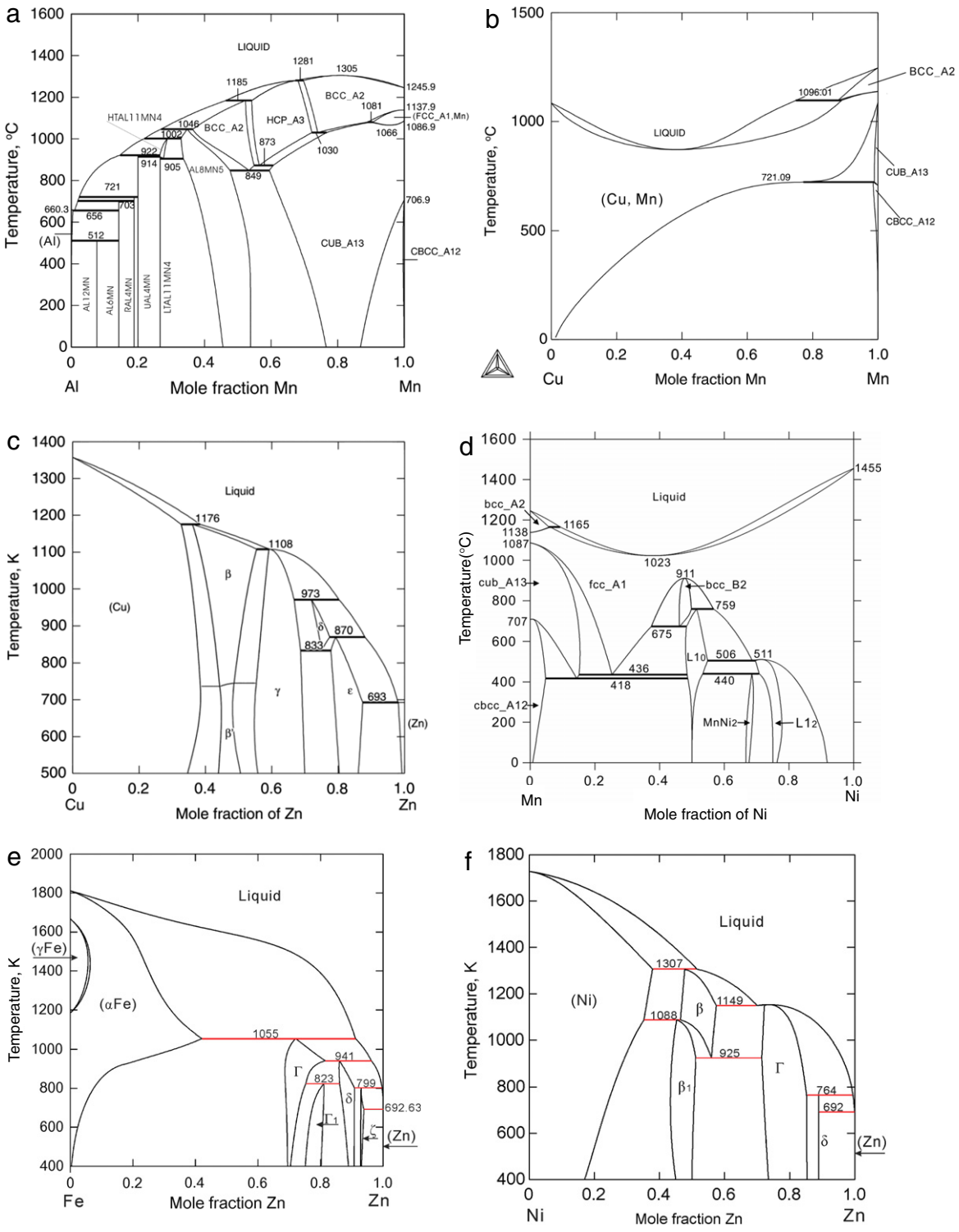

Fig. 14. Calculated Al–Mn phase diagram [31], (b) Calculated Cu–Mn phase diagram [110], (c) Calculated Cu–Zn phase diagram [111], (d) Calculated Mn–Ni phase diagram [101], (e) Calculated Fe–Zn phase diagram [112], (f) Calculated Ni–Zn phase diagram [113].

peritectic reaction since neither XRD pattern nor microstructure is presented [138].

The key contributions to the understanding of the phase equilibria in the Al-rich corner of the Al–Fe–Mn–Si system are the work by Davignon et al. [139], who analyzed 19 quaternary alloys using optical microscopy and EPMA. Confirming the previous investigations [5,23,130,134], Davignon et al. [139] found that β-AlFeSi dissolves about 0.5 at.% Mn at 550 °C. In contradiction to the previously mentioned authors [5,23,130,134], they [139] claimed that the solubility of Fe in α-AlMnSi is up to 12 at.% at 550 °C.

Using the equilibrium constant for the reaction leading to the formation of the quaternary phase $Al_8FeMnSi_2$, Flores-Valdes et al. [140] derived the Gibbs energy of formation for this quaternary phase. On the basis of EDX microprobe analysis of the precipitated solid phases, Onderka et al. [141] found the existence of another quaternary phase $Al_{11.8}FeMn_{1.6}Si_{1.6}$. This quaternary phase is not included in the thermodynamic optimization since

Table 1
Comparison between calculated and measured invariant equilibria in Al-rich part of the quaternary Al–Fe–Mg–Mn system.

Source	Liquid composition (wt%Fe,	wt%Mg,	wt%Mn)	T (°C)
	Liq + (Fe, Mn)Al_6 = (Al) + $Al_{13}Fe_4$ + $Mg_3Mn_2Al_{18}$			
Calculated (this work)	0.002	33	0.002	457
Measured [130]	<1	~30	~0.5	446
	Liq = (Al) + AlMg-β + $Al_{13}Fe_4$ + $Mg_3Mn_2Al_{18}$			
Calculated (this work)	0.001	33.8	0.001	450
Measured [130]	<1	~32	~0.3	~445

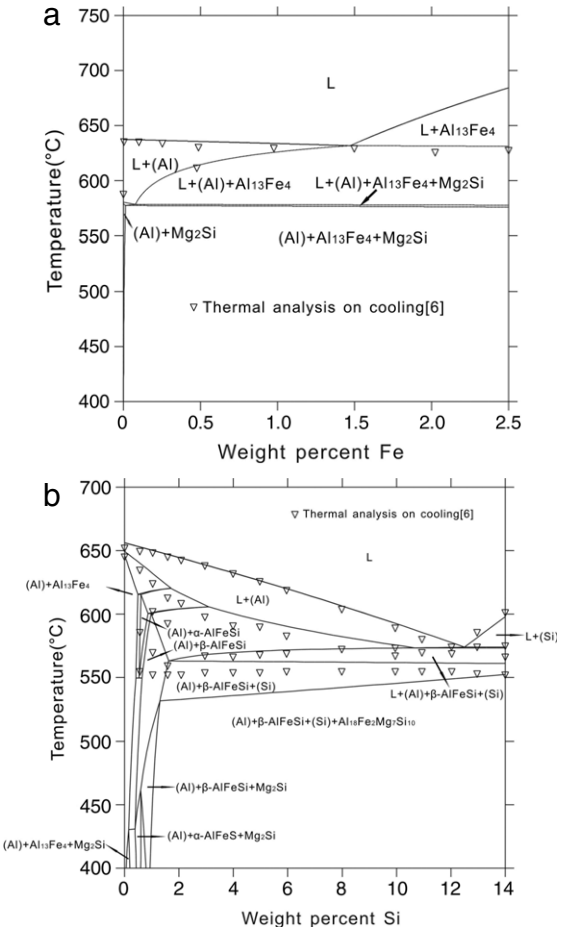

Fig. 15. (a) Calculated vertical section at 4 wt% Mg and 0.5 wt%. Si in the Al–Fe–Mg–Si system along with the experimental data [6], (b). Calculated vertical section at 0.5 wt% Mg and 0.5 wt% Fe in the Al–Fe–Mg–Si system along with the experimental data [6].

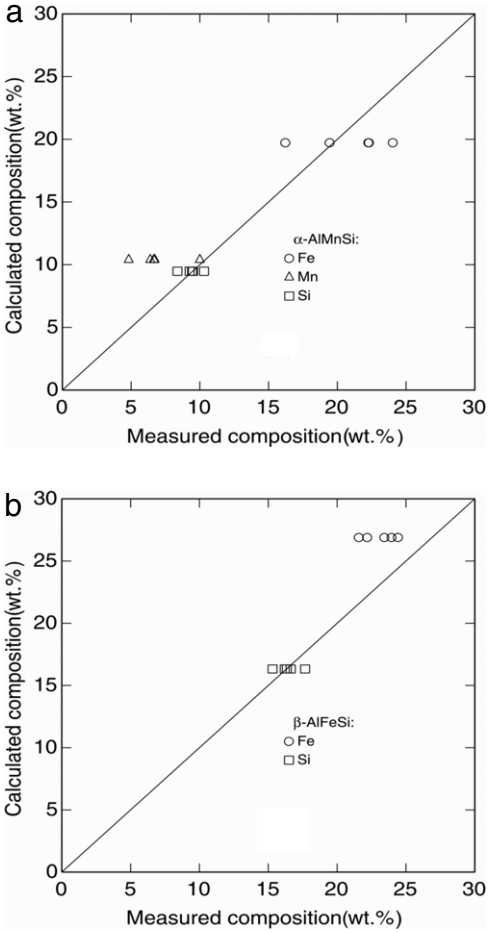

Fig. 16. Calculated compositions for α-AlMnSi and β-AlFeSi in the four-phase equilibrium region ((Al), (Si), α-AlMnSi and β-AlFeSi), compared with the experimental values of [139]: (a) α-AlMnSi and (b) β-AlFeSi.

there is no experimental information on its equilibrium with any other phases.

In the present work, the thermodynamic parameters for the phases $Al_8FeMnSi_2$, α-AlMnSi, and β-AlFeSi are evaluated by considering the invariant reaction data [5,23,134], the melting temperature of the quaternary phase $Al_8FeMnSi_2$ [138], and the phase assemblage data [139]. In view of the large solubility for Fe in α-AlMnSi, this phase is described with the sublattice model $Al_{14}(Fe, Mn)_4(Al, Si)_5$. In order to reduce the number of adjustable parameters, it is assumed that Fe only substitutes for Mn in the second sublattice.

The optimized thermodynamic parameters in the Al–Fe–Mn–Si quaternary system are presented elsewhere [101]. The computed and observed invariant reactions are presented in Table 3, showing reasonable agreement for most of the reactions. Fig. 16 compares the calculated compositions for α-AlMnSi and β-AlFeSi at 550 °C in the four-phase region ((Al), (Si), α-AlMnSi, and β-AlFeSi) with the measured values from Davignon et al. [139]. The fit to the experimental data is reasonable. All of the measured [139] phase assemblages (i.e., (Al) + (Si) + α-AlMnSi + β-AlFeSi, (Al) + (Si) + α-AlMnSi, (Al) + α-AlMnSi, (Al) + α-AlMnSi + $Al_{13}Fe_4$, and (Al) + $Al_{13}Fe_4$ + Al_6Mn) are confirmed by the present modeling. A further check on the reliability of the thermodynamic modeling is provided in Fig. 17, where the model-predicted liquidus temperatures along six vertical sections are compared with the corresponding experimental values from Zakharov et al. [23,134]. It is demonstrated that the experimental data are reasonably described by the thermodynamic calculation although they are not included in the thermodynamic modeling.

5.4. Al–Mg–Mn–Si

No quaternary phases were found in the Al–Mg–Mn–Si quaternary system [15]. The thermodynamic properties for the system

Table 2
Comparison between calculated and measured invariant equilibria in Al-rich part of the quaternary Al–Fe–Mg–Si system.

Source	Liquid composition (wt%Fe,	wt%Mg,	wt%Si)	T (°C)
	$L + (Al) + Mg_2Si + Al_{13}Fe_4 = \alpha$-AlFeSi			
Calculated (this work)	0.47,	9.22,	6.68	580
Measured [6]	1.35,	7.25,	7.05	586
	$L + (Al) + Mg_2Si + \alpha$-AlFeSi $= \beta$-AlFeSi			
Calculated (this work)	0.47,	8.36,	7.89	577
Measured [6]	0.82,	6.45,	9.80	576
	$L + (Al) + Mg_2Si + \beta$-AlFeSi $= \pi(Al_{18}Fe_2Mg_7Si_{10})$			
Calculated (this work)	0.39,	7.40,	9.58	570
Measured [6]	0.55,	6.00,	11.40	568
	$L + \beta$-AlFeSi $= (Al) + (Si) + \pi(Al_{18}Fe_2Mg_7Si_{10})$			
Calculated (this work)	0.34,	3.85,	12.93	560
Measured [6]	0.52,	2.90,	12.15	567
	$L = (Al) + (Si) + Mg_2Si + \pi(Al_{18}Fe_2Mg_7Si_{10})$			
Calculated (this work)	0.064,	5.88,	13.26	553
Measured [6]	0.15,	4.90,	12.90	555
	$L = (Al) + Al_8Mg_5 + Mg_2Si + Al_{13}Fe_4$			
Calculated (this work)	0.002,	33.95,	0.14	450
Measured [6]	0.11,	33.30,	0.35	451
Measured [131]				447

Table 3
Comparison between calculated and measured invariant equilibria in Al-rich part of the quaternary Al–Fe–Mn–Si system.

Source	Liquid composition (wt%Fe,	wt%Mg,	wt%Si)	T (°C)
	$L = (Al) + (Si) + \alpha$-AlMnSi $+ \beta$-AlFeSi			
Calculated (this work)	0.59	0.21	12.49	575
Measured [5]	0.70	0.14	12.63	574
Measured [130]	~0.6	~0.2	11.70	565
	$L = (Al) + (Si) + Al_8FeMnSi_2$			
Calculated (this work)	0.35	0.43	12.56	575
Measured [134]	0.36	0.40	12.40	576
	$L = (Al) + (Si) + Al_8FeMnSi_2 + \alpha$-AlMnSi			
Calculated (this work)	0.32	0.48	12.58	575
Measured [134]	0.17	0.52	12.40	575
	$Liq + Al_{13}Fe_4 = (Al) + \alpha$-AlMnSi $+ \alpha$-AlFeSi			
Calculated (this work)	1.6	1.0	3.96	629.5
Measured [130]	~2.5	~0.2	~4	<630
	$Liq + \alpha$-AlFeSi $= (Al) + \alpha$-AlMnSi $+ \beta$-AlFeSi			
Calculated (this work)	1.41	0.73	7.0	611
Measured [130]	~1.5	~0.3	~7	~600

are synthesized from the descriptions of the constituent ternary systems. Table 4 shows the comparison between the calculated and measured invariant equilibria [130], which indicates reasonable fit to the experimental data.

5.5. Fe–Mg–Mn–Si

There is no experimental information on the Fe–Mg–Mn–Si system in the literature. Consequently, the thermodynamic properties for this quaternary system are synthesized from the descriptions of the ternary systems.

5.6. Al–Fe–Mg–Mn–Si

Using TA and microstructure observation techniques, Barlock and Mondolfo [130] found that the eutectic reaction $L = (Al) + Al_3Fe + Al_8Mg_5 + Mg_2Si + Al_8Mg_2Mn_2$ occurs at 445 °C. By using the established thermodynamic database, the computed temperature for this eutectic reaction is 450 °C, which agrees reasonably with the measured temperature [130].

Du et al. [142] performed the DSC measurements for Al 356.1 sample annealed at 500 °C for 45 days under high vacuum in a quartz tube (10^{-4} bar). The obtained first transition temperature on the DSC heating curve is at 575 °C. The computed temperature for the reaction $L \Leftrightarrow (Al) + (Si) + \beta$-AlFeSi $+ \alpha$-AlMnSi is at 575 °C. This excellent agreement is an additional evidence for the reliability of the presently established thermodynamic database in the Al–Fe–Mg–Mn–Si quinary system.

Using an integrated approach of key experiments and thermodynamic modeling, supplemented with first-principles calculations, we have established a new thermodynamic database for multicomponent Al alloys. The new database contains all the important Al-based alloys, and in total 345 solution and intermetallic phases are included in this database [143]. Numerous calculations on different kinds of commercial alloys show a very good accuracy of the database for both the prediction of the phases formed and the temperature for formation. Solidification simulations using Scheil model are shown for various kinds of commercial Al alloys, showing a good agreement with the experimental data.

6. Summary

In this paper, an overview on the investigation of phase diagram and thermodynamics of technologically important Al alloys is made with an emphasis on a need of the integrated

Table 4
Comparison between calculated and measured invariant equilibria in Al-rich part of the quaternary Al–Mg–Mn–Si system.

Source	Liquid composition (wt%Mg,	wt%Mn,	wt%Si)	T (°C)
	Liq + α-AlMnSi = (Al) + Al_6Mn + Mg2Si			
Calculated (this work)	16.2	0.15	2.1	567
Measured [130]	~30	~0.3	~0.5	~630
	Liq = (Al) + Mg_2Si + (Si) + α-AlMnSi			
Calculated (this work)	5.8	0.16	13.3	553
Measured [130]	<5	<0.1	~1.2	548
	Liq = (Al) + AlMg-β + Mg_2Si + $Mg_3Mn_2Al_{18}$			
Calculated (this work)	33.95	0.001	0.14	449.8
Measured [130]	~30	~0.1	~0.2	~445
	Liq + Al_6Mn = (Al) + Mg_2Si + $Mg_3Mn_2Al_{18}$			
Calculated (this work)	23.8	0.027	0.67	524
Measured [130]	<30	~0.1	~0.2	

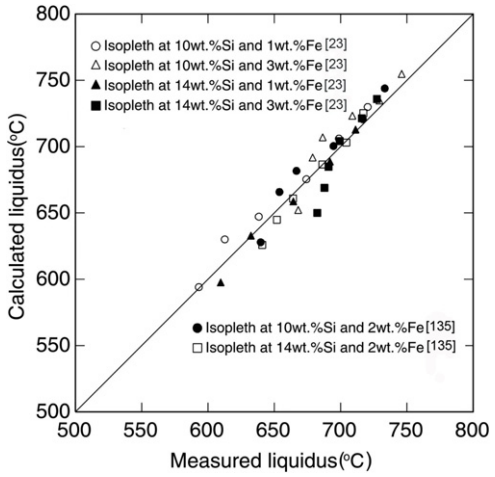

Fig. 17. Calculated liquidus temperatures in the Al–Fe–Mn–Si system with the experimental data from Zakharov et al. [23,134]. These experimental data are not used in the evaluation of the parameters.

approach. Such an integrated approach is the combination of key experiments and thermodynamic modeling, supplemented with first-principles calculations. Thus, the major experimental methods, which are widely employed to provide phase diagram and thermodynamic data, are briefly described. In addition, the basics of the first-principles calculations and CALPHAD are presented focusing on the link of these two computational approaches. Such a link can provide fundamental information, which is usually not accessible experimentally, and thus can supplement the thermodynamic database. A case study for the representative Al–Fe–Ni ternary system is demonstrated in order to corroborate the developed hybrid approach, followed by a brief introduction to our current activities on investigations of phase diagrams in multicomponent Al alloys. The present thermodynamic database for the multicomponent Al alloys can cover much wider composition and temperature ranges than the previous Al databases.

Acknowledgments

The present work is supported by the National Basic Research Program of China (Grant No. 2011CB610401), Creative Research Group of National Natural Science Foundation of China (Grant No. 51021063), National Natural Science Foundation of China (Grant No. 50831007), and Science Center for Phase Diagrams & Materials Design and Manufacture of Central South University of China. The authors would like to thank the students and researchers at Science Center for Phase Diagrams & Materials Design and Manufacture, Central South University of China for their diligent work, particularly Dr. H.L. Chen, Dr. C.Y. He, Dr. Z. Pan, Dr. W. Xiong, Dr. C.Y. Tang Dr. J.L. Liang, J. Wang, W.H. Sun, P.S. Wang, J.R. Zhao, B. Hu, Dr. Yi Kong, W.W. Zhang, K.K. Chang, H.L. Yan, C.S. Sha, and Kai Li. The valuable comments from the reviewers are appreciated.

Appendix. Supplementary data

Supplementary material related to this article can be found online at doi:10.1016/j.calphad.2011.06.007.

References

[1] Thermo-Calc, http://www.thermocalc.com/.
[2] Pandat, http://www.computherm.com/pandat.html.
[3] H.W.L. Phillips, J. Inst. Met. 68 (1942) 27–46.
[4] H.W.L. Phillips, J. Inst. Met. 69 (1943) 275–350.
[5] H.W.L. Phillips, M.P.C. Varley, J. Inst. Met. 69 (1943) 317–350.
[6] H.W.L. Phillips, J. Inst. Met. 72 (1946) 151–227.
[7] E.H. Dix Jr., Trans. AIME 69 (1923) 957–971.
[8] E.H. Dix Jr., A.C. Heath Jr., Trans. AIME, Inst. Met. Div. (1928) 164–197.
[9] A.G.C. Gwyer, H.W.L. Phillips, J. Inst. Met. 38 (1927) 29–83.
[10] G. Masing, O. Dahl, Wiss. Veroff. Siemens-Konzern 8 (1929) 248–251.
[11] Von V. Fuss, Z. Met.kd. 23 (1931) 231–236.
[12] H. Bückle, Aluminium-Archiv. 13 (1938) 1–18.
[13] A.J. Bradley, A. Taylor, J. Inst. Met. 66 (1940) 53–63.
[14] H.P. Takeda, K. Mutuzaki, Tetsu-to-Hagane 26 (1940) 335–361.
[15] G. Phragmen, J. Inst. Met. 77 (1950) 489–552.
[16] G.V. Raynor, P.C.L. Pfeil, J. Inst. Met. 73 (1947) 397–419.
[17] J.N. Pratt, G.V. Raynor, J. Inst. Met. 79 (1951) 211–232.
[18] H. Nowotny, K. Komarek, J. Kromer, Berg. Hüttenmannische Monatsh. Hochsch. Leoben 96 (8) (1951) 161–169.
[19] Y. Du, J.C. Schuster, F. Weitzer, N. Krendelsberger, B.Y. Huang, Z.P. Jin, W.P. Gong, Z.H. Yuan, H.H. Xu, Metall. Mater. Trans. A 35A (2004) 1613–1628.
[20] Landolt-Börnstein, http://www.springerlink.com, Germany, 2010.
[21] I. Ansara, COST 507-Definition of Thermochemical and Thermophysical Properties to Provide a Database for the Development of New Light Alloys, vol. 1, COST Secretariat, Brussels, Belgium, 1998.
[22] N.A. Belov, D.G. Eskin, A.A. Aksenov, Multicomponent Phase Diagrams: Applications for Commercial Aluminum Alloys, Elsevier, 2005.
[23] A.M. Zakharov, I.T. Gul'din, A.A. Arnol'd, Yu.A. Matsenko, Izv. Vyssh, Uchebn. Zaved, Tsvetn. Metall. 4 (1988) 89–94.
[24] G. Davignon, A. Serneels, B. Verlinden, L. Delaey, Metall. Mater. Trans. A 27 (1996) 3357–3361.
[25] N. Krendelsberger, F. Weitzer, J.C. Schuster, Metall. Mater. Trans. A 33A (2002) 3311–3319.
[26] K.W. Richter, H. Ipser, Intermetallics 11 (2003) 101–109.
[27] K. Chandrasekaran, K.W. Richter, H. Ipser, Intermetallics 14 (2006) 491–497.
[28] Y. Du, J.C. Schuster, Z.–K. Liu, R.X. Hu, P. Nash, W.H. Sun, W.W. Zhang, J. Wang, L.J. Zhang, C.Y. Tang, Z.J. Zhu, S.H. Liu, Y.F. Ouyang, W.Q. Zhang, N. Krendelsberger, Intermetallics 16 (2008) 554–570.
[29] L.J. Zhang, J. Wang, Y. Du, R.X. Hu, P. Nash, X.-G. Lu, C. Jiang, Acta Mater. 57 (2009) 5324–5341.
[30] W. Xiong, Y. Du, J. Wang, W.-W. Zhang, X.-G. Lu, Int. J. Mater. Res. 99 (6) (2008) 598–612.
[31] Y. Du, J. Wang, J.R. Zhou, J.C. Schuster, R. Schmid-Fetzer, M. Ohno, Z.-K. Liu, S.L. Shang, H.H. Xu, W.Q. Zhang, Int. J. Mater. Res. 98 (9) (2007) 855–871.
[32] L. Kaufman, H. Nesor, Computer Calculation of Phase Diagrams, Academic Press, New York, 1970.
[33] M. Hillert, Phase equilibria, in: Phase Diagrams and Phase Transformations: Their Thermodynamic Basis, Cambridge University Press, 1998.

[34] M. Asta, V. Ozolins, C.A. Woodward, JOM (September) (2001) 16–19.
[35] P.E.A. Turchi, I.A. Abrikosov, B. Burton, S.G. Fries, G. Grimvall, L. Kaufman, P. Korzhavyi, V.R. Manga, M. Ohno, A. Pisch, A. Scott, W.Q. Zhang, CALPHAD 31 (2007) 4–27.
[36] C. Wolverton, X.-Y. Yan, R. Vijayaraghavan, V. Ozoliņš, Acta Mater. 50 (2002) 2187–2197.
[37] C. Wolverton, V. Ozoliņš, Phys. Rev. B 73 (2006) 144104/1–14.
[38] W.J. Golumbfskie, R. Arroyave, D. Shin, Z.-K. Liu, Acta Mater. 54 (2006) 2291–2304.
[39] Z.-K. Liu, J. Phase Equilib. Diffus. 30 (5) (2009) 517–534.
[40] J.-C. Zhao, Methods for Phase Diagram Determination, Elsevier, USA, 2007.
[41] O. Kubaschewski, C.B. Alcock, P.J. Spencer, Materials Thermochemistry, sixth ed., Pergamon Press, 1993.
[42] J.V. Gilfrich, I.C. Noyan, T.C. Huang, R. Jenkins, D.K. Smith, P.K. Predecki, Advances in X-ray Analysis, Springer, 1997.
[43] W. Massa, Crystal Structure Determination, Springer, 2000.
[44] R. Vogel, Z. Anorg. Chem. 107 (1919) 265–307.
[45] M.L.V. Gayler, J. Inst. Met. 29 (1923) 507–528.
[46] J. Goldstein, D.E. Newbury, D.C. Joy, P. Echlin, C.E. Lyman, E. Lifshin, Scanning Electron Microscopy and X-ray Microanalysis, Springer, 2003.
[47] S.J.B. Reed, Electron Microprobe Analysis and Scanning Electron Microscopy in Geology, Cambridge University Press, 1996.
[48] C.Y. He, Y. Du, H.-L. Chen, P.S. Wang, H.W. Ouyang, Int. J. Mater. Res. 99 (8) (2008) 907–911.
[49] H.-L. Chen, F. Weitzer, J.C. Schuster, Y. Du, H.H. Xu, J. Alloy. Compd. 436 (2007) 313–318.
[50] H.H. Xu, Y. Du, Y.C. Zhou, X.J. Zheng, W. Xiong, S.H. Liu, X.P. Su, F.C. Yin, Int. J. Mater. Res. 99 (6) (2008) 644–649.
[51] H.H. Xu, Y. Du, B.Y. Huang, Z.P. Jin, S.T. Li, X. Zhang, Z. Met.kd. 97 (2) (2006) 140–144.
[52] H.H. Xu, Y. Du, Y.H. Tan, Y.H. He, S.T. Li, X. Zhang, J. Alloy. Compd. 425 (2006) 153–158.
[53] Y. Du, H.H. Xu, Y.C. Zhou, Y.F. Ouyang, Z.P. Jin, Mater. Sci. Eng. A 448 (2007) 210–215.
[54] H.H. Xu, Y. Du, Y.C. Zhou, X.J. Zheng, W. Xiong, S.H. Liu, X.P. Su, F.C. Yin, Int. J. Mater. Res. 99 (6) (2008) 644–649.
[55] H.H. Xu, X. Xiong, L.J. Zhang, Y. Du, P.S. Wang, Metall. Mater. Trans. A 40A (9) (2009) 2042–2047.
[56] Z.P. Jin, Scand. J. Metall. 10 (1981) 279–287.
[57] M.E. Brown, Introduction to Thermal Analysis: Techniques and Applications, Springer, 2001.
[58] Y. Du, J.C. Schuster, Y.A. Chang, J. Mater. Sci. 40 (4) (2005) 1023–1025.
[59] A.E. Miller, A.H. Daane, C.E. Habermann, B.J. Beaudry, Rev. Sci. Instr. 34 (1963) 644–647.
[60] R. Capelli, S. Delfino, A. Saccone, A. Borsese, R. Ferro, Thermochimica Acta 28 (1979) 113–119.
[61] S. Delfino, R. Ferro, R. Capelli, A. Borsese, Z. Met.kd. 65 (1974) 781–783.
[62] S. Delfino, R. Ferro, R. Capelli, A. Borsese, J. Less-Common Met. 41 (1975) 59–64.
[63] G. Rambaldi, D. Mazzone, R. Marazza, S. Delfino, R. Ferro, J. Less-Common Met. 59 (1978) 201–210.
[64] D. Mirković, R. Schmid-Fetzer, Z. Met.kd. 97 (2006) 119–129.
[65] O.J. Kleppa, J. Phase Equilib. 15 (1994) 240–263.
[66] R.X. Hu, P. Nash, J. Mater. Sci. 41 (2006) 631–641.
[67] Y.B. Kim, F. Sommer, B. Predel, J. Alloy Compd. 247 (1997) 43–51.
[68] A. Pisch, F. Hodaj, P. Chaudouët, C. Colinet, J. Alloys Compd. 319 (2001) 210–213.
[69] F. Sommer, G. Borzone, N. Parodi, R. Ferro, Intermetallics 14 (2006) 287–296.
[70] H.N. Su, P. Nash, Z.-K. Liu, in: O. Elizabeth, H. Peggy, W. Eric, P. Bernard, M. Toshio (Eds.), High Temperature Corrosion and Materials Chemistry, IV, Electrochemical Society, Inc., Pennington (NJ), 2003.
[71] S.-L. Shang, Y. Wang, D.E. Kim, Z.-K. Liu, Comput. Mater. Sci 47 (2009) 1040–1048.
[72] Y. Wang, Z.-K. Liu, L-Q. Chen, Acta Mater. 52 (2004) 2665–2671.
[73] H. Zhang, S.L. Shang, Y. Wang, A. Saengdeejing, L.-Q. Chen, Z.-K. Liu, Acta Mater. 58 (2010) 4012–4018.
[74] J.P. Perdew, Y. Wang, Phys. Rev. B 45 (1992) 13244–13248.
[75] J.P. Perdew, K. Burke, M. Ernzerhof, Phys. Rev. Lett. 77 (1996) 3865–3868.
[76] J.P. Perdew, A. Zunger, Phys. Rev. B 23 (1981) 5048–5079.
[77] G. Kresse, J. Furthmuller, Phys. Rev. B 54 (1996) 11169–11186.
[78] G. Kresse, D. Joubert, Phys. Rev. B 59 (1999) 1758–1775.
[79] G. Grimvall, Thermophysical Properties of Materials, Amsterdam, North-Holland, 1999.
[80] S.L. Shang, Y. Wang, Z.K. Liu, Phys. Rev. B 82 (2010) 014425.
[81] J.W.D. Connolly, A.R. Williams, Phys. Rev. B 27 (1983) 5169–5172.
[82] S. Shang, A. Böttger, Acta Mater. 53 (2005) 255–264.
[83] Y. Wang, Z.K. Liu, L.Q. Chen, Acta Mater. 52 (2004) 2665–2671.
[84] S.L. Shang, Y. Wang, Z.K. Liu, Phys. Rev. B 75 (2007) 024302.
[85] S.L. Shang, Y. Wang, D. Kim, Z.K. Liu, Comput. Mater. Sci. 47 (2010) 1040–1048.
[86] F. Körmann, A. Dick, B. Grabowski, B. Hallstedt, T. Hickel, J. Neugebauer, Phys. Rev. B 78 (2008) 033102.
[87] S. Khmelevskyi, I. Turek, P. Mohn, Phys. Rev. Lett. 91 (2003) 037201.
[88] I.A. Abrikosov, A.E. Kissavos, F. Liot, B. Alling, S.I. Simak, O. Peil, A.V. Ruban, Phys. Rev. B 76 (2007) 014434.
[89] B. Alling, T. Marten, I.A. Abrikosov, Nature Mater. 9 (2010) 283–284.
[90] A. Zunger, S.H. Wei, L.G. Ferreira, J.E. Bernard, Phys. Rev. Lett. 65 (1990) 353–356.
[91] Y. Wang, L.G. Hector, H. Zhang, S.L. Shang, L.Q. Chen, Z.K. Liu, Phys. Rev. B 78 (2008) 104113.
[92] Y. Wang, S.L. Shang, H. Zhang, L.Q. Chen, Z.K. Liu, Philos. Mag. Lett. 90 (2010) 851–859.
[93] J.-O. Andersson, T. Helander, L. Höglund, P.F. Shi, B. Sundman, CALPHAD 26 (2) (2002) 273–312.
[94] S.-L. Chen, S. Daniel, F. Zhang, Y.A. Chang, X.-Y. Yan, F.-Y. Xie, R. Schmid-Fetzer, W.A. Oates, CALPHAD 26 (2) (2002) 175–188.
[95] C.W. Bale, P. Chartrand, S.A. Degterov, G. Eriksson, K. Hack, R. Ben Mahfoud, J. Melancon, A.D. Pelton, S. Petersen, CALPHAD 26 (2) (2002) 189–228.
[96] R.H. Davies, A.T. Dinsdale, J.A. Gisby, J.A.J. Robinson, S.M. Martin, CALPHAD 26 (2) (2002) 229–271.
[97] N. Dupin, I. Ansara, B. Sundman, CALPHAD 25 (2001) 279–298.
[98] B. Sundman, I. Ohnuma, N. Dupin, U.R. Kattner, S.G. Fries, Acta Mater. 57 (2009) 2896–2908.
[99] X.G. Lu, B. Sundman, J. Ågren, CALPHAD 33 (2009) 450–456.
[100] J. De Keyzer, G. Cacciamani, N. Dupin, P. Wollants, CALPHAD 33 (2009) 109–123.
[101] S.H. Liu, Ph.D thesis, Central South University, China, 2010.
[102] I. Ansara, N. Dupin, H.L. Lukas, B. Sundman, J. Alloys Compd. 247 (1997) 20–30.
[103] L.J. Zhang, Y. Du, H.H. Xu, S.H. Liu, Y.J. Liu, F. Zheng, H.Y. Zhou, C.Y. Tang, Int. J. Mater. Res. 100 (2009) 160–165.
[104] I. Chumak, K.W. Richter, H. Ipser, Intermetallics 15 (2007) 1416–1424.
[105] I. Chumak, K.W. Richter, S.G. Fries, H. Ipser, J. Phase Equilib. Diffus. 28 (2007) 417–421.
[106] I. Chumak, K.W. Richter, H. Ipser, J. Phase Equilib. Diffus. 29 (2008) 300–304.
[107] L.J. Zhang, Y. Du, CALPHAD 31 (2007) 529–540.
[108] L.J. Zhang, Y. Du, H.H. Xu, C.Y. Tang, H.L. Chen, W.Q. Zhang, J. Alloys Compd. 454 (2008) 129–135.
[109] M. Albers, D. Kath, K. Hilpert, Metall. Mater. Trans. A 27A (1996) 3569–3575.
[110] C.Y. He, Y. Du, H.L. Chen, S.H. Liu, H.H. Xu, Y.F. Quyang, Z.-K. Liu, J. Alloy Compd. 457 (2008) 233–238.
[111] J. Wang, H.H. Xu, S.L. Shang, L.J. Zhang, Y. Du, W.Q. Zhang, S.H. Liu, P.S. Wang, Z.-K. Liu, CALPHAD 35 (2011) 191–203.
[112] W. Xiong, Y. Kong, Y. Du, Z.-K. Liu, M. Selleby, W.H. Sun, CALPHAD 33 (2) (2009) 433–440.
[113] W. Xiong, H.H. Xu, Y. Du, CALPHAD 35 (3) (2011) 276–283.
[114] P. Liang, H.-L. Su, P. Donnadieu, M.G. Harmelin, A. Quivy, P. Ochin, G. Effenberg, H.J. Seifert, H.L. Lukas, F. Aldinger, Z. Met.kd. 89 (1998) 536–540.
[115] X.Y. Yan, Y.A. Chang, J. Alloy Compd. 308 (2000) 221–229.
[116] C. Servant, B. Sundman, O. Lyon, CALPHAD 25 (2001) 79–95.
[117] J. Gröbner, D. Mirković, M. Ohno, R. Schmid-Fetzer, J. Phase Equilib. Diffus. 26 (3) (2005) 234–239.
[118] M.H.G. Jacobs, P.J. Spencer, CALPHAD 22 (4) (1998) 513–525.
[119] D. Kevorkov, R. Schmid-Fetzer, J. Phase Equilib. 25 (2) (2004) 140–151.
[120] J. Miettinen, CALPHAD 28 (3) (2004) 313–320.
[121] J.C. Schuster, Y. Du, Metall. Mater.Trans. A 31A (7) (2000) 1795–1803.
[122] C.Y. He, Y. Du, H.L. Chen, H.H. Xu, CALPHAD 33 (2009) 200–210.
[123] H.L. Chen, Ph.D thesis, Central South University, China, 2008.
[124] H.L. Chen, Y. Du, H.H. Xu, W. Xiong, L.J. Zhang, L. Chen, J. Mater. Res. 24 (10) (2009) 3154–3164.
[125] Z.J. Zhu, Master Thesis, Central South University, China, 2008.
[126] P.S. Wang, J.R. Zhao, Y. Du, H.H. Xu, T. Gang, J.C. Fen, L.J. Zhang, C.Y. He, S.H. Liu, H.W. Ouyang, Int. J. Mater. Res. 102 (2011) 6–16.
[127] Y. Du, J.R. Zhao, C. Zhang, H.L. Chen, L.J. Zhang, J. Mining Metall. 43B (2007) 39–56.
[128] Z. Pan, Ph.D. Thesis, Central South University, China, 2008.
[129] M. Wang, P.S. Wang, S.H. Liu, Y. Du, H.H. Xu, W.Q. Zhang, CALPHAD 35 (2) (2011) 183–190.
[130] J.G. Barlock, L.F. Mondolfo, Z. Met.kd. 66 (1975) 605–611.
[131] I.T. Gul'din, N.V. Dokukina, Zh. Neorg. Khim. 3 (1958) 799–814.
[132] R. Krendelsberger, P. Rogl, A. Leithe-Jasper, C.J. Simensen, J. Alloys Compd. 264 (1998) 236–239.
[133] H. Nowotny, W. Marquardt, Mikroskopie 3 (1949) 71–83.
[134] A.M. Zakharov, I.T. Gul'din, A.A. Arnol'd, Yu.A. Matsenko, Russ. Metall. 4 (1989) 89–94.
[135] H. Thoresen, J.A. Horst, J. Tibballs, Peritectic precipitation of α-Al (Fe, Mn) Si from the melt, Senter for Industriforskning, Report N 890222-1, Oslo, 1991.
[136] C. Simensen, T. Rolfsen, J. Tibballs, Determination of the lattice parameter of α-Al(Fe, Mn)Si crystals, Senter for Industriforskning, Report N 890222-2, Oslo, 1991.
[137] C. Simensen, A. Bjorneklett, Model for α-AlMnSi and α-Al(Fe, Mn)Si, Senter for Industriforskning, Report N 890222-4, Oslo 1991.
[138] A. Flores-Valdes, M.I. Pech-Canul, M. Mendez-Nonell, M. Sukiennik, Scripta Metall. 30 (1994) 435–439.
[139] G. Davignon, A. Serneels, B. Verlinden, L. Delaey, Metall. Mater. Trans. A 27 (1996) 3357–3361.
[140] A. Flores-Valdes, M. Sukiennik, A.H. Castillejos-E, F.A. Acosta-G, J.C. Escobedo-B, Intermetallics 6 (1998) 217–227.
[141] B. Onderka, M. Sukiennik, K. Fitzner, Arch. Metall. 45 (2000) 119–132.
[142] Y. Du, Y.A. Chang, S.H. Liu, B.Y. Huang, F.-Y. Xie, Y. Yang, S.-L. Chen, Z. Met.kd. 96 (2005) 1351–1362.
[143] A. Markström, Y. Du, S.H. Liu, L.J. Zhang, L. Kjellqvisrt, J. Bratberg, A. Engström, TCAL1: a new thermodynamic database for aluminium alloys, CALPHAD XL, May 22–27, 2011, Rio de Janeiro, Brazil.